Ore Geology Reviews 139 (2021) 104509

Contents lists available at ScienceDirect

Ore Geology Reviews

journal homepage: www.elsevier.com/locate/oregeorev

Melt volatile budgets and magma evolution revealed by diverse apatite halogen and trace elements compositions: A case study at Pulang porphyry Cu-Au deposit, China

Shaoying Zhang[a], Liqiang Yang[a,*], Wenyan He[a], Xue Gao[a], Xudong Liu[a,b]

[a] State Key Laboratory of Geological Processes and Mineral Resources, China University of Geosciences, Beijing 100083, China
[b] Beijing Institute of Geological Survey, Beijing 102206, China

ARTICLE INFO

Keywords:
Apatite inclusion
Volatiles
Trace elements
Magma mixing
Pulang porphyry Cu-Au deposit

ABSTRACT

Apatites those shielded as inclusions in igneous minerals are avoided of diffusion effects associated with evolving melts and can record the original volatile and trace element evolutions of the magma. Volatile and trace element compositions of apatites enclosed in high-Al, medium-Al, low-Al amphibole, magmatic biotite, plagioclase, and groundmass from ores, quartz monzonite porphyry (QMP) and its mafic microgranular enclaves (MMEs), and pre-ore coarse-grained quartz diorite porphyry (CQD) were present to evaluate the magmatic processes in the formation of Pulang porphyry Cu-Au deposit. All apatite inclusions are magmatic fluorapatites and occur as early-crystallization phases (940–980 °C), followed by the crystallization sequence of high-Al amphibole, medium-Al amphibole, magmatic biotite, plagioclase, low-Al amphibole (altered medium-Al amphibole) with fluctuating fO_2 conditions. Compared to the low SO_3 (<0.27 wt%) concentrations of other apatites inclusions in fertile QMP, the biotite-hosted apatites retain an abnormal SO_3 (0.15–1.01 wt%) and Cl (0.08–0.71 wt%) enrichment. Estimates of sulfur and chlorine concentrations using partitioning models for apatite in QMP return similar features, where the biotite-hosted apatites yield highly variable melt S (315–2025 ppm) and Cl (0.1–1.2 wt%) contents. The presence of biotite-hosted S-Cl enriched apatites with overgrowth texture, together with the resorbed medium-Al amphiboles in QMP, both suggest that they have crystallized from an extra sulfur supplement process caused by the injection of a series of S-Cl enriched magma, and even subsequent remelting of the preexisting dioritic batholith and its interior apatites. Such magma processes further account for the fluid exsolution and alteration from medium-Al amphiboles to low-Al ones. Whereas, those from the barren CQD systematically returns normal SO_3 (0.18–0.70 wt%) and Cl (0.03–0.51 wt%) concentrations with estimates of melt S (335–1321 ppm) and Cl (0.1–0.5 wt%) contents exhibiting features of typical arc basalts (300–1000 ppm; 0.01–0.85 wt%, respectively). Although the acicular apatite of MMEs has normal SO_3 contents (0.19–0.37 wt%), its abundance also confirm an extra sulfur supplement process. The altered apatites of both QMP and CQD showing pitted surface with visible voids and LREE-rich mineral inclusions return low SO_3 (<0.06 wt%) and Cl (<0.22 wt%) concentrations, indicating that these elements were depleted during potassic and phyllic alteration.

Given that Sr/Y ratios (2.21–3.62) of apatite at Pulang do not vary significantly with changing melt composition (Mg = 119.1–528.8 ppm), the Sr/Y and Eu/Eu* ratios of apatite from QMP have confirmed a water-rich, oxidized magma origin, whereas the CQD are originated from a water-poor, reduced source. Besides, the hydrothermal alteration possibly accounts for the abnormally increased Ce/Ce* ratios of altered apatites from CQD and decreased Sr/Y ratios of the low-Al amphibole-hosted apatite from QMP. Therefore, using trace elements as indicators for petrogenetic studies would be more robust for those apatites enclosed in igneous minerals. Our studies demonstrate that apatite inclusions can be linked to discrete periods in the crystallization history of its host phases, thus providing insight into the magma evolution process.

* Corresponding author.
E-mail address: lqyang@cugb.edu.cn (Y. Liqiang).

https://doi.org/10.1016/j.oregeorev.2021.104509
Received 18 March 2021; Received in revised form 28 September 2021; Accepted 28 September 2021
Available online 2 October 2021

1. Introduction

Open magmatic processes, such as magma mixing and degassing, are critical to the hypogene porphyry copper deposits, both in the enrichment of copper and its precipitation as sulfide (Hedenquist and Lowenstern, 1994; Sillitoe, 2010). The change from copper transport to copper precipitation is normally attributed to an abrupt change in those intensive parameters such as pH, oxygen fugacity, temperature, and pressure (Landtwing et al., 2005; Proffett, 2009; Sillitoe, 2010) or an external Sulphur source in the form of gases from volatile-rich mafic magmas (Blundy et al., 2015) or by the mafic magma itself (Hattori and Keith, 2001; Maughan et al., 2002; Caricchi et al., 2014) in deeper reservoirs. Therefore, evaluating the behavior of volatile and nonvolatile elements, including trace elements, during the magmatic-hydrothermal processes is crucial to solving the question that whether a single magmatic fluid responding to changing physical conditions or a superimposed process involving multiple sulfur sources can attribute to the formation of giant porphyry deposits. The magmatic volatiles are usually investigated through melt inclusions, which are not always available and sometimes not large enough for in-situ analysis. Besides, the melt inclusions can be easily modified by the post-crystallization processes or volatiles diffusion during magma ascent (e.g., Qin et al., 1992; Lloyd et al., 2013).

Apatite [$Ca_{10}(PO_4)_6(F,Cl,OH)_2$], as an alternative indicator of melt volatile/trace element contents and inheritor of their variations with magma evolution, is a nearly ubiquitous accessory phase in terrestrial (Webster and Piccoli, 2015) and extraterrestrial (McCubbin and Jones, 2015) geological systems and can structurally incorporate a broad range of elements, including volatile (e.g., S, Cl, OH, F) (Webster and Piccoli, 2015; Riker et al., 2018) and redox-sensitive elements (e.g., Eu, Ce) (Hughes and Rakovan, 2002; Pan and Fleet, 2002; Prowatke and Klemme, 2006). Therefore, Apatite chemistry has been exploited to constrain volatile compositions of fluids/melts relevant to eruptive, pluton-building, and mineralizing processes in volcanic systems (e.g., Chelle-Michou and Chiaradia, 2017; Stock et al., 2018; Li et al., 2020b). In addition, trace elements in apatite also serve as a unique magmatic fingerprint providing important information on igneous provenance and volcanic tephrochronology as well as for the exploration for mineral deposits (e.g., Jennings et al., 2011; Mao et al., 2016; Bruand et al., 2017; Nathwani et al., 2020; Gao et al., 2020). Particularly, experiments have shown that volatiles (S, Cl, F) are fast-diffusive elements (Li et al., 2020a), and therefore indicate that if volatiles have not been significantly exchanged with a surrounding phase (fluid, melt, or volatile-bearing mineral) after the crystallization of apatite, any initial volatiles zoning acquired during crystal growth should fade away and homogenize within weeks (Chelle-Michou and Chiaradia, 2017; Sato et al., 2017; Li et al., 2020a). Such features would be utilized for the assessment of volatile mixing in case of the development of volatiles-zoning.

The Pulang Cu-Au porphyry deposit, located in the East Tethys metallogenic belt, is a newly discovered giant porphyry Cu-Au deposit. Previous researches on apatite at Pulang have provided details on magmatic fertility, petrogenesis, and source evolution of its host porphyries (e.g., Pan et al., 2016, 2020; Xing et al., 2018; Gao et al., 2020). However, the lack of temporal and spatial descriptions of the apatite and its host minerals does not adequately explain the melt volatiles and trace elements behaviors, especially during the late magmatic-hydrothermal translation stage. Here, we present halogens and trace elements concentrations of apatite inclusions shielded in various amphiboles, magmatic biotite, plagioclase, and groundmass from the pre-ore coarse-grained quartz diorite porphyry (CQD), *syn*-ore quartz monzonite porphyry (QMP), and enclosed mafic microgranular enclaves (MMEs) at Pulang. Petrographical and chemical analyses of apatite inclusions and their hosted minerals are used to elucidate volatile evolution and trace element behavior in open magmatic processes.

2. Regional geology

The NNW-trending Yidun Terrane is located between the western Songpan-Garze Fold Belt and the eastern Qiangtang Terrane, bounded by the eastern Garze-Litang Suture Zone and the western Jinshajiang Suture Zone, and the Yangtze Craton to the southeast (Fig. 1a, b). The N-S-trending Fault then cuts the Yidun Terrane into two areas, the western Zhongza Block and the eastern Yidun arc (Hou et al., 2003; Deng et al., 2014a). The Zhongza Block is composed of deformed and metamorphosed Paleozoic rocks (Reid et al., 2007). The Yidun arc mainly comprises Late Triassic arc-like magmatic rocks (238–210 Ma; Li et al., 2011) and coeval volcaniclastic rocks, which intrude or conformably overlie Middle-Upper Triassic fine-grained clastic, bioclastic, and mudstone rocks (Reid et al., 2007).

In the southern Yidun arc (namely the Zhongdian arc; Fig. 1c), the exposed Upper Triassic strata of the Qugasi and Tumugou formations comprise clastic and volcanic rocks with carbonate, sandstone, and slate interlayers (Hou et al., 2007). Late Triassic porphyry intrusions mainly comprise quartz dioritic, monzonitic and granodioritic porphyry (ca. 228–206 Ma; Leng et al., 2014; Cao et al., 2016) and intrude the Upper Triassic strata. These porphyries have similar initial $^{87}Sr/^{86}Sr$ ratios (0.7058–0.7077) and εNd values (−1.88 to −1.93), and highly fractionated REE patterns with high Sr/Y ratios, resembling adakitic signatures (Wang et al., 2011). These porphyries are supposed to be derived from partial melting of the metasomatized asthenospheric mantle wedge (Hou et al., 1993; Wang et al., 2011; Deng et al., 2014a; Yang et al., 2017; Leng et al., 2018). However, recent works also propose the possibility of reactivating the Neoproterozoic arc root (Wang et al., 2021). Although characterized by minor exposed area, these porphyries host several porphyry deposits, including the Pulang (4.18 Mt Cu with average grades of 0.50–0.53%), Xuejiping (0.28 Mt with 0.53%), Lannitang (0.18 Mt with 0.50%), Disuga, Chundu and other deposits (Fig. 1c). These deposits have identically exposed strata and porphyry intrusions (Li et al., 2019b; Yang and Cooke, 2019) but different hydrothermal alteration zonations, especially those in the Pulang and Xuejiping deposit (Leng et al., 2012; Cao et al., 2019).

A series of NW-SE-oriented sinistral strike-slip faults develop across the Yidun arc (Fig. 1b, c; Hou et al., 2003; Deng et al., 2014b). Mesozoic intrusions are elongated NW-SE, parallel to the adjacent fault systems, and commonly show ductile to brittle deformation along their margins, but relatively undeformed at their centers, of which the magmatic lineations and flow structures are generally subparallel to each other (Yang et al., 2016).

3. Deposit geology and characteristics of apatite inclusions

3.1. Ore geology

The Pulang deposit is located at 28°02′19″N–99°59′23″E, at an altitude of over 3300 m (Fig. 2), and is the largest and best-documented deposit in the Zhongdian Cu belt (Li et al., 2011; Fan and Li, 2006). It is inferred to contain 804 Mt at 0.52% Cu and 0.18 g/t Au (Li et al., 2011). Pulang now has three mineralized centers, namely South, East, and North Pulang (Fig. 2). Particularly, South Pulang is the most important of these, containing 98% of the total Cu-Au reserves in the deposit. East and North Pulang contain sparse Cu-Au-bearing veins (Fig. 2; Cao et al., 2019; Yang and Cooke, 2019).

Two main geological units are present in the ore district, including the Early-Triassic sedimentary rocks and Late-Triassic porphyry intrusions (Fig. 2). The former accounts for 70% of the surface outcrop across the whole ore district, and the latter comprises three major porphyry intrusions with an outcrop area of ~8.9 km^2. Early Triassic sedimentary rocks at Pulang include the Tumugou Formation, which comprises two members, T_3t^1 and T_3t^2. T_3t^1 comprises black carbonaceous slate, andesite, and metasandstone, with a total thickness of >2700 m, and is mainly distributed in the east (Fig. 2). T_3t^2 comprises

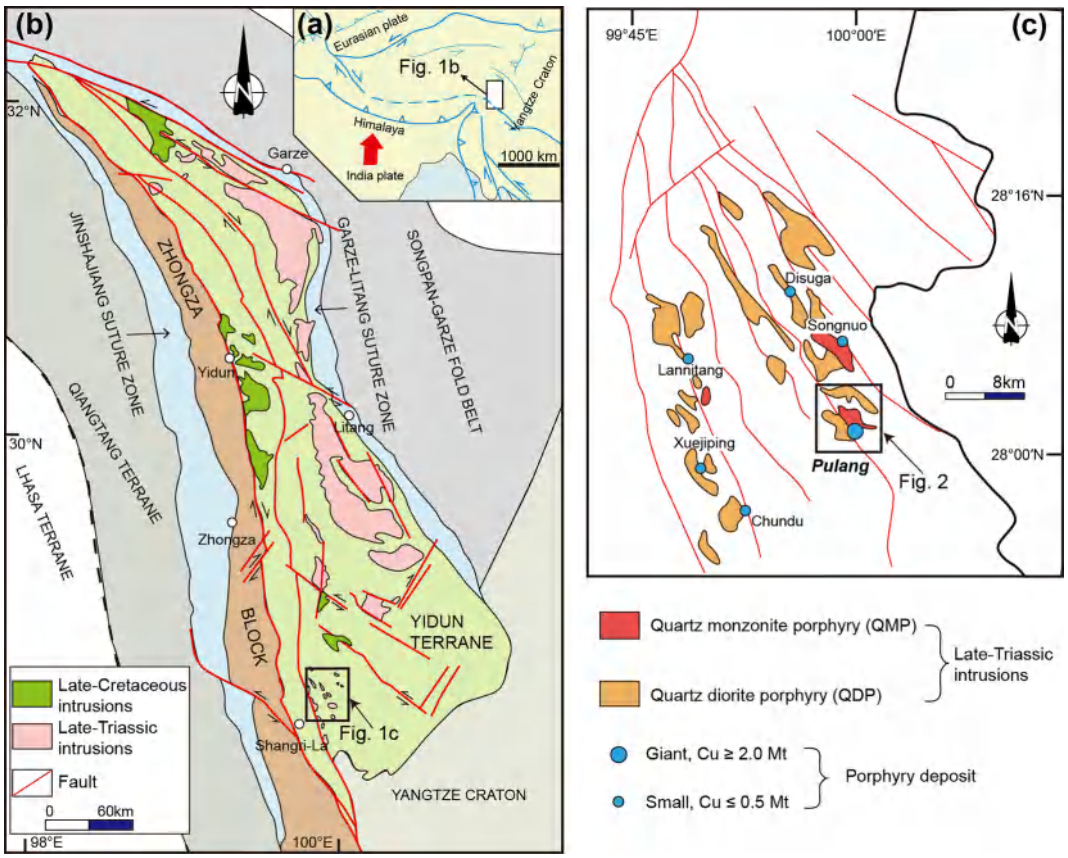

Fig. 1. *(a)* Tectonic outline of the India and Eurasia collision zone and *(b)* the Yidun arc (simplified from Yang et al., 2018); *(c)* Simplified geological map of the southern portion of the Yidun arc (modified after Li et al., 2017).

black carbonaceous slate with euhedral pyrite, carbonaceous phyllite, metasandstone, and bedded limestone, with a total thickness of >680 m, and mainly distributed in the west of the Pulang deposit (Fig. 2). There are four porphyry stocks in the ore district, including pre-ore fine-grained quartz diorite porphyry (FQD, ca. 218.7 ± 6.3 Ma) and coarse-grained quartz diorite porphyry (CQD, 211–224 Ma), *syn*-ore quartz monzonite porphyry (QMP, 211–218 Ma), and post-ore granite porphyry (GP, ca. 208 Ma) intrusions (see detailed reviews in Cao et al., 2019). The greenish-gray FQD crops out ~0.7 km^2 at North Pulang and occasionally at some drill holes at South and East Pulang (Cao et al., 2019). Its phenocryst mainly includes plagioclase and groundmass consist of plagioclase, amphibole, and little quartz, with minor mineralization and alteration (Cao et al., 2019). The CQD is the most voluminous intrusion in the deposit and crops out over ~9.0 km^2 (Fig. 2). Phenocrysts include plagioclase (~5 vol%), biotite (~5 vol%), amphibole (~3 vol%), and minor K-feldspar (<2 vol%), which account for ~15 vol% of the rock volume (Fig. 3a). Its groundmass consists of more mafic minerals (mostly magmatic biotite) than the FQD and shows grayish color (Fig. 3a). The QMP intrudes the center of the CQD and outcrops over an area of ~0.5 km^2 at South Pulang (Fig. 2). Compared to the CQD, the QMP is dominated by quartz (~15 vol%), K-feldspar (~10 vol%), biotite (~8 vol%), plagioclase (~5 vol%), and minor amphibole (~2 vol%), which account for 30 vol% of the rock volume (Fig. 3b). Its groundmass comprises much more silicate and less mafic minerals than the CQD and exhibits lighter color (Fig. 3b). A series of mafic microgranular enclaves (MMEs) occur in the QMP (Fig. 3c) and have been reported in the CQD (Liu et al., 2015; Cao et al., 2018). These enclaves are 5–15 cm in size and exhibit elliptic and irregular occurrence, with occasionally plastic deformation (Fig. 3c). Phenocrysts in the MMEs exhibit smaller grains with quenched edges and much more magmatic biotite than those of the CQD and QMP. It represents biotite (~15 vol%), amphibole (~5 vol%), quartz (~5 vol%), K-feldspar (~3 vol%), plagioclase (~2 vol%), and accounts for 30 vol% of the rock (Fig. 3c). Its groundmass also consists of plenty of mafic minerals and shows dark-green color (Fig. 3c). Phenocrysts of the GP include k-feldspar and quartz and the groundmass consists of plagioclase, k-feldspar, quartz, and biotite, with minor pyrite (Wang et al., 2018). Additionally, a suit of simultaneous diorite porphyries (DP; ca. 216 Ma) has also been reported as dikes at the northeast part of the deposit (Cao et al., 2018). Phenocrysts within the DP are primarily plagioclase, amphibole, and biotite, and the groundmass comprises feldspar and quartz, with minor amphibole and biotite. Accessory minerals within the FQD, CQD, QMP, and MMEs, DP are dominantly apatite, titanite, zircon, and magnetite (Fig. 2; Cao et al., 2018, 2019; Li et al., 2019b). As the CQD and QMP in the South Pulang make up the vast majority of the Pulang intrusive complex, the paper herein mainly focuses on the CQD, QMP, and MMEs.

Hydrothermal alteration in Pulang has been characterized by concentric zones varying from an inner potassic zone outward through a sericitic zone to an outer propylitic zone (Fan and Li, 2006; Li et al., 2011). However, recent investigations argue that the zoned alteration is not clear as previously thought, since propylitic/sericitic alteration extensively invades the core potassic zone (Cao et al., 2019). Potassic alteration, which generally occurs in or near the centers of porphyry systems (Sillitoe, 2010), is mostly developed in the QMP, and partly overprinted by later propylitic alteration (Fig. 4a). Propylitic alteration, characterized by chlorite, epidote, and locally chalcopyrite, pyrite, calcite, strongly overprinted early potassic alteration at South Pulang (Fig. 4a). Besides, silica alteration occurs centrally within the potassic alteration of the causative QMP, implying a possible hydrothermal-mineralization center (Fig. 4b). Phyllic alteration typically occurs as selectively pervasive replacement of feldspars and mafic minerals by fine-grained sericite (illite) or as vein halos (Fig. 4c). Phyllic alteration is

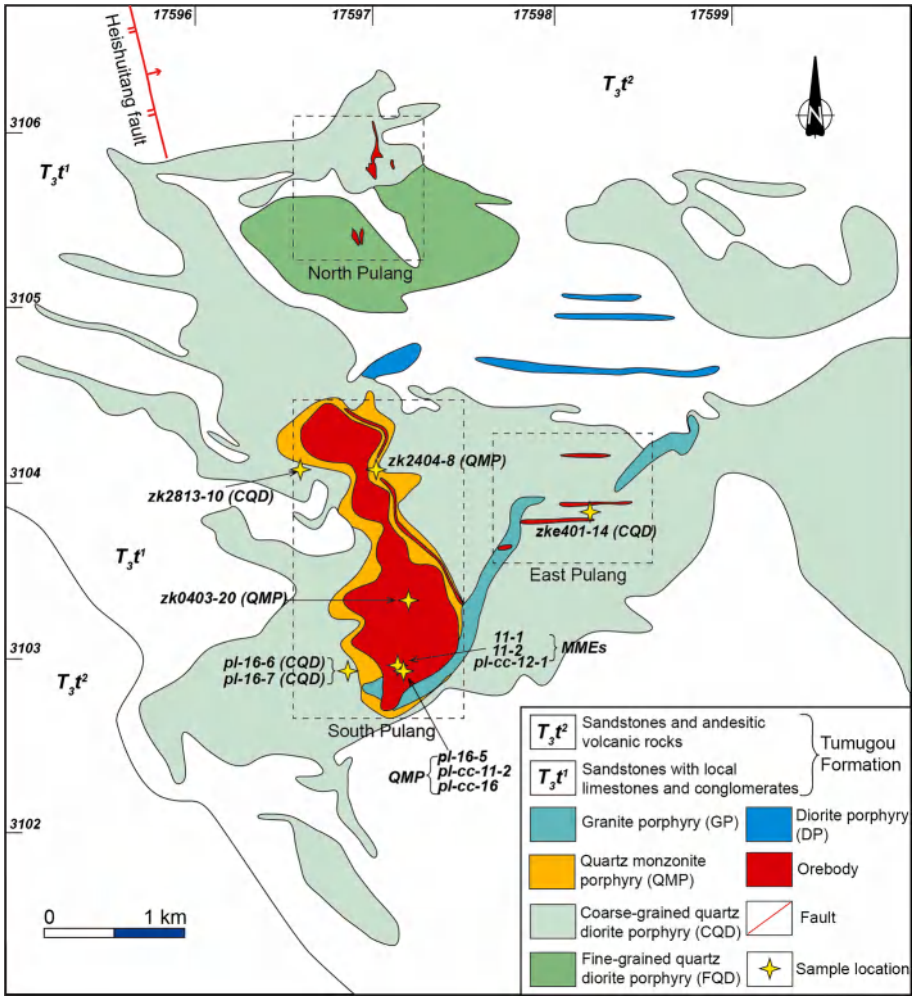

Fig. 2. Simplified geological map of the Pulang Cu-Au deposit, showing major lithology units and sample locations (modified from Cao et al., 2019).

structurally controlled and occurs pervasively within the fracture zones of the QMP (Fig. 4c). The veins associated with potassic alteration consist mainly of the early-stage k-feldspar + quartz alteration and late-stage biotite + quartz ± chalcopyrite ± pyrite veins (Fig. 4b). Veins associated with propylitic alteration include quartz + chlorite + epidote + chalcopyrite ± pyrite ± calcite (Fig. 4d). Veinlet, stockwork, and disseminated Cu-Au ores are primarily hosted within the QMP and are featured by an assemblage of chalcopyrite + pyrite ± bornite ± molybdenite (Fig. 4d). Chalcopyrite is disseminated or fills fractures and mainly occurs in veins associated with chlorite + epidote, which has been invaded by late-stage quartz + minor pyrite ± chalcopyrite veins and cuts through the early-stage biotite-quartz veins (Fig. 4d).

The NW-trending Heishuitang fault is the major structures in the deposit (Fig. 2). This fault dips 42° to 65° northeast and extends for at least 10 km across the central part of the district. The above CQD and QMP both are emplaced into the core of the Pulang anticline, generally along the Heishuitang fault. The GP is inferred to be emplaced along the blind ENE-trending fault, which only crops out locally but is obvious in satellite images (Fan and Li, 2006).

3.2. Features of apatite and host minerals

Apatite of the CQD, QMP, and MMEs can be roughly divided into six types based on various host minerals: (1) apatite in high-Al amphibole; (2) apatite in medium-Al amphibole; (3) apatite in low-Al amphibole; (4) apatite in magmatic biotite; (5) apatite in plagioclase; (6) apatite in groundmass (Figs. 5–7).

Three types of amphibole phenocrysts containing apatite inclusions are documented in the CQD, high-Al, medium-Al, and low-Al amphiboles (Fig. 5a, b, c). High-Al amphiboles (Al_2O_3 = 8.56–12.02 wt%; Supplementary Table S1) are brown, subhedral to euhedral, and range in size from 50 to 300 μm (Fig. 5a). Apatite in high-Al amphibole occurs as homogeneous grains 30–200 μm in diameter, with both equant and elongated habits. Those equant apatite inclusions coeval with k-feldspar have a remarkable low S and Cl contents, whereas the isolated and slightly elongated apatite inclusions are marked with higher S contents (1.01 wt%; Fig. 5a). Most medium-Al amphiboles (Al_2O_3 = 5.83–7.85 wt %) of CQD have euhedral and larger phenocrysts, and occasionally inclusions of pyrite (Fig. 5b). Apatite in medium-Al amphibole is euhedral, inclusion-free and transparent. Additionally, BSE images reveal that the medium-Al amphibole encompasses the high-Al amphiboles, or is enclosed by the high-Al ones (Fig. 5d, e). The low-Al amphiboles (Al_2O_3 = 2.08–3.03 wt%) of CQD are tabular and green in color, and occasionally coexist with epidote or chlorite, showing hydrothermal features in origin. Besides, the enclosed apatite is anhedral and contains substantial fluid inclusions (Fig. 5c). Magmatic biotite phenocrysts of CQD are fresh, dark-brown, euhedral, and ranges in size from 0.2 to 0.7 mm (Fig. 5f). They are almost free of alteration and microscale deformation in the core, but some of which are altered to chlorite on their edges (Fig. 5f). Much more apatite inclusions are present in biotites than in amphiboles and are characterized by inhomogeneous patches and visible voids due to hydrothermal alteration, where the altered zone has lower S contents and the primary core has higher S contents (Fig. 5g). The plagioclase of CQD is mostly subhedral to euhedral, 0.5–2 mm in

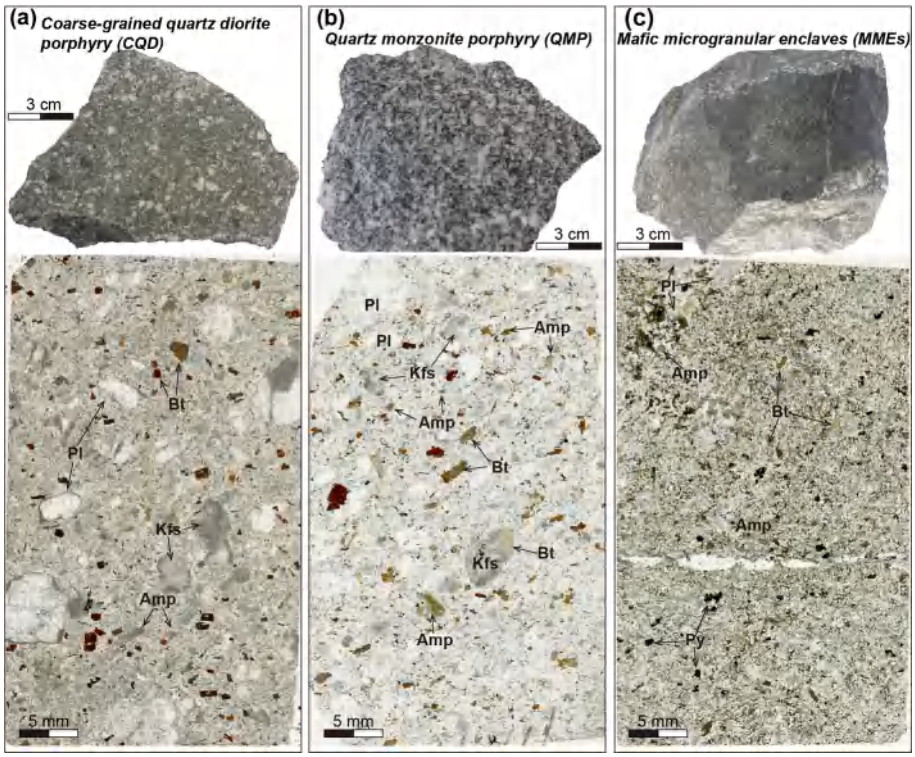

Fig. 3. Scanned sections and hand specimen of research samples. *(a)* coarse-grained quartz diorite porphyry (pl16-6), and its groundmass consists of more mafic minerals; *(b)* quartz monzonite porphyry (pl-cc-11–2) and *(c)* mafic microgranular enclaves (pl-cc-12–1), with smaller grains and quenched edges. Amp-amphibole, Bt-biotite, Pl-plagioclase, Kfs-k-feldspar, Chl-chlorite, Qtz-quartz, Py-pyrite.

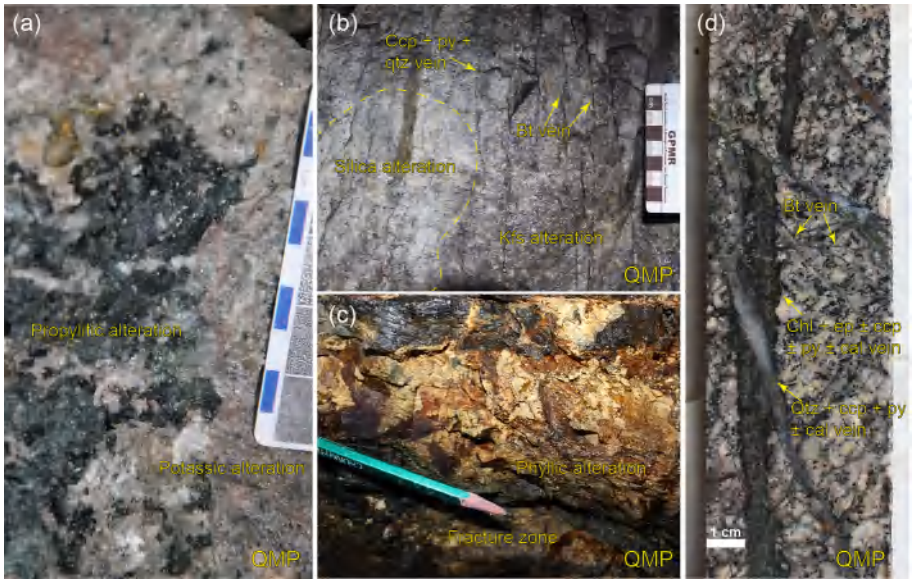

Fig. 4. Photographs of hydrothermal alteration and vein types in Pulang. *(a)* propylitic alteration overprint potassic alteration; *(b)* Biotite vein and chalcopyrite + pyrite + quartz vein intrude the k-feldspar alteration and silica alteration core; *(c)* well developed phyllic alteration in fracture zone; *(d)* chlorite + epidote ± chalcopyrite ± pyrite ± calcite vein cut through early biotite vein and cut by later quartz + chalcopyrite + pyrite ± calcite vein. Ccp-chalcopyrite, Ep-epidote, Cal-calcite.

size, and has weak zonation, with polysynthetic twinning developed (Fig. 5h). Illite or sericite aggregates have been developed on the surface of plagioclases and the enclosed apatite inclusions are mostly elongated and contain obvious fluid inclusions (Fig. 5h). Apatite inclusions in the groundmass of CQD usually display pitted surface and irregular edges, with assemblages of chlorite and pyrite (Fig. 5i).

None high-Al amphiboles have been observed in QMP, especially those which have apatite inclusions enclosed. The medium-Al amphiboles (Al_2O_3 = 6.11–7.09 wt%) of QMP are euhedral and large, with occasionally resorbed textures developed (Fig. 6a). Magmatic biotite, plagioclase, titanite, and pyrite also occur as fillers in the resorbed caves (Fig. 6a). Additionally, some medium-Al amphiboles have been altered to low-Al amphiboles along its edge due to the hydrothermal influence (Fig. 6b, c). Under BSE images, the low-Al amphiboles act as irregular plaques in the medium-Al amphiboles, indicating that these low-Al amphiboles are hydrothermal instead of magmatic origin (Fig. 6b). Similarly, low-Al amphibole-hosted apatite inclusions have been affected by hydrothermal fluid, leaving the dark and jagged edges behind (Fig. 6d). More magmatic biotites containing apatites exist in QMP and these biotites are relatively fresh, euhedral, light- to dark-

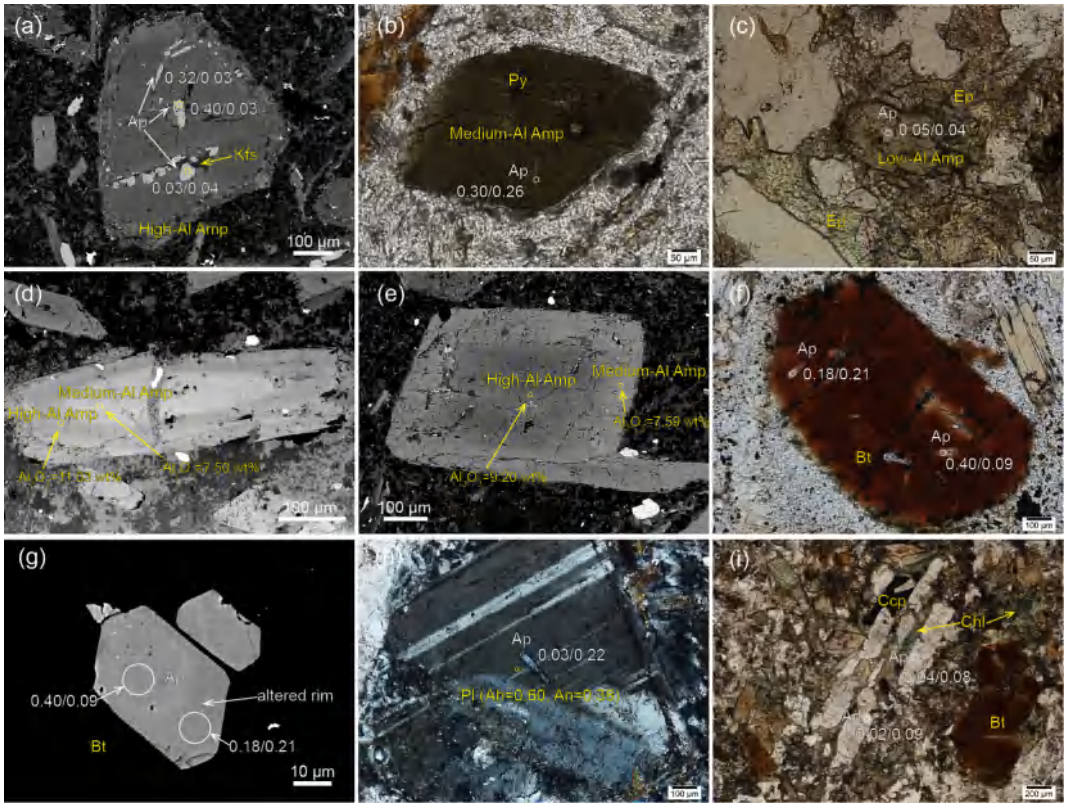

Fig. 5. Photomicrographs of apatite inclusions enclosed at igneous minerals in coarse-grained quartz diorite porphyry. White circles represent the analyzed spots and concentrations of SO_3 and Cl in apatite crystals are shown in wt% (SO_3/Cl). *(a)* apatite in high-Al amphibole and occasionally coexisting with k-feldspar; *(b)* apatite in medium-Al amphibole, with pyrite; *(c)* apatite in low-Al amphibole, surrounded with epidote; *(d)* high-Al amphibole encloses medium-Al amphibole; *(e)* medium-Al amphibole encloses high-Al amphibole; *(f)* apatite in magmatic biotite; *(g)* biotite-enclosed apatite have core-rim texture due to hydrothermal alteration; *(h)* apatite in plagioclase with polysynthetic twin; *(i)* irregular apatite in the groundmass, coexist with chlorite. Amp-amphibole, Kfs-k-feldspar, Bt-biotite, Pl-plagioclase, Qtz-quartz, Ep-epidote, Chl-chlorite, Ap-apatite, Py-pyrite, Ccp-chalcopyrite.

brown, with little hydrothermal alteration (Fig. 6e). These biotites may occur as inclusions in low-Al amphibole (Fig. 6c). The enclosed apatite inclusions are elongated or stubby, and generally inclusion-free as resolved by BSE imaging, and range from 10 to 130 μm (Fig. 6f). However, some of these apatites have also been affected by hydrothermal fluids as inhomogeneous patches partly replace the irregular crystal (Fig. 6g). The host feldspars of QMP are 0.5 to 2 mm in size, tabular, and subhedral to euhedral, similar to those of CQD (Fig. 6h). The hosted apatite inclusions are transparent, elongated to stubby, with sizes ranging from 20 to 150 μm. Compared to those in CQP, fewer fluid inclusions have been observed on their surfaces (Fig. 6h). Similarly, the apatite inclusions in the groundmass of CQD show partly altered features and obvious core-rim textures, where the altered rim shows visible voids and darker color and the original zone show lighter color (Fig. 6i).

Elongated medium- (Al_2O_3 = 6.51–6.89 wt%) and low-Al amphiboles (Al_2O_3 = 3.46–3.84 wt%) occur as aggregations in the MMEs, where only the low-Al ones have visible apatite inclusions (Fig. 7a). Additionally, selective replacement of low-Al amphibole by chlorite aggregates in MMEs are present as a result of propylitic alteration (Fig. 7b). The apatite inclusions in low-Al amphibole of MMEs commonly have irregular crystal shapes and inhomogeneous patches, coexisting with pyrite (Fig. 7c). Two types of magmatic biotites have been observed in MMEs: (1) the biotites enclosing apatites have normally worn and uneven edges and (2) the elongated and euhedral biotites have no apatites (Fig. 7d). These morphological features indicate that the irregular biotites are likely captured from the host QMP or CQD, whereas the elongated ones are formed due to undercooling. The apatite inclusions in biotites commonly have irregular crystal shapes and inhomogeneous patches, leaving the unaltered magmatic cores (Fig. 7e). Much more acicular apatite inclusions in the groundmass of MMEs are present, compared with the stubby apatite inclusions of the biotites and amphiboles (Fig. 7f). Similarly, the acicular apatites are probably the results of fast growth due to undercooling.

In summary, apatite-bearing high-Al amphiboles occur mainly in CQD, and the high-Al and medium-Al amphiboles enclose each other, suggesting that the high-Al and medium-Al amphiboles could co-crystallize in a magma mixing event. The main magmatic minerals in CQD, QMP, and MMEs exhibit similar crystallization sequences, which are, high-Al amphibole, medium-Al amphibole, magmatic biotite, plagioclase, low-Al amphibole (altered medium-Al amphibole), from early to late.

4. Sampling, analytical, and calculation methods

4.1. Sampling

Five relatively fresh rock samples of QMP (pl-cc-11-2, pl-16-5, pl-cc-16, zk0403-20, zk2404-8), four of CQD (pl-16-6, pl-16-7, zk2813-10, zke401-14), and three of MMEs (pl-cc-12-1, 11-1, 11-2) were polished to several thin sections along different orientations. All these sections were then scanned to hunt for those under the minimum effect of hydrothermal alteration. The selected sections were carefully analyzed by microscope before elemental analyses. Sample locations are marked in Fig. 2.

4.2. Analytical methods

94 apatite inclusions, 76 amphiboles, 21 biotites, and 6 plagioclases

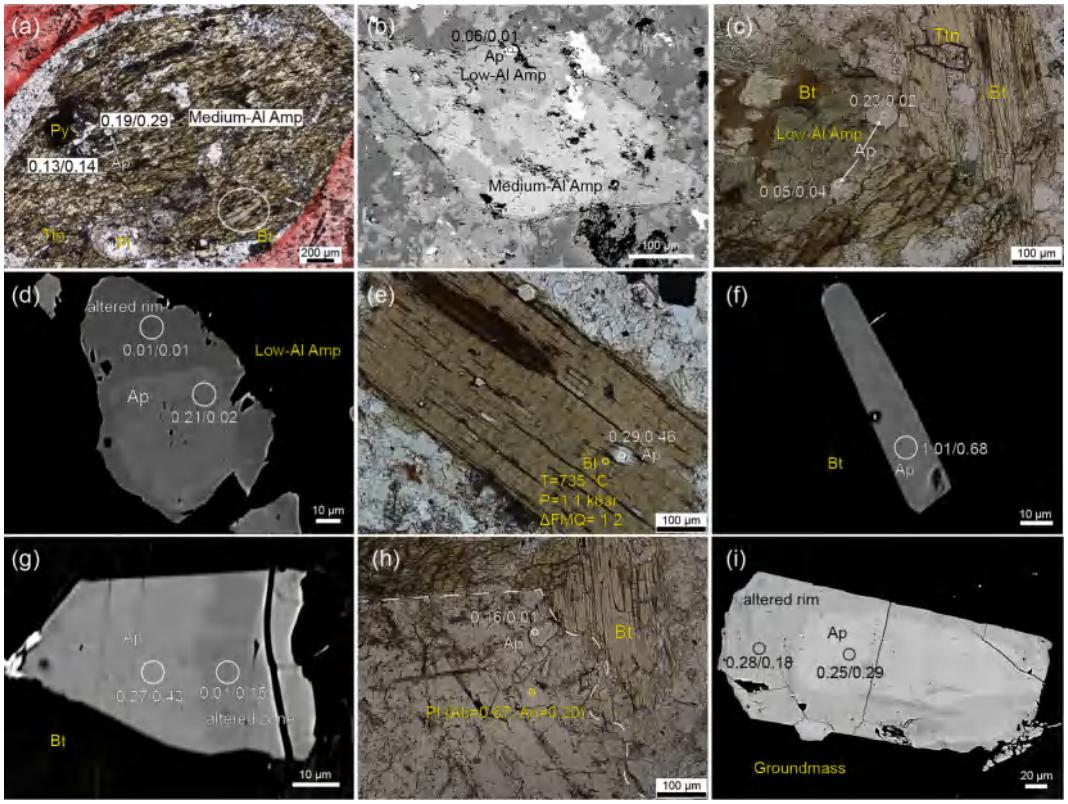

Fig. 6. Photomicrographs of apatite inclusions enclosed at igneous minerals in quartz monzonite porphyry. *(a)* resorbed medium-Al amphibole with magmatic biotite, apatite, plagioclase, titanite, and pyrite as fillers; *(b)* medium-Al amphibole altered to low-Al amphibole, with dark patches; *(c)* magmatic biotite and apatite enclosed in altered low-Al amphibole; *(d)* partly altered apatite inclusion in low-Al amphibole; *(e)* apatite in fresh magmatic biotite; *(f)* primary apatite in magmatic biotite; *(g)* partly altered apatite in biotite, showing zoned alteration; *(h)* apatite in plagioclase; *(i)* apatite in the groundmass, with clearly altered rim.

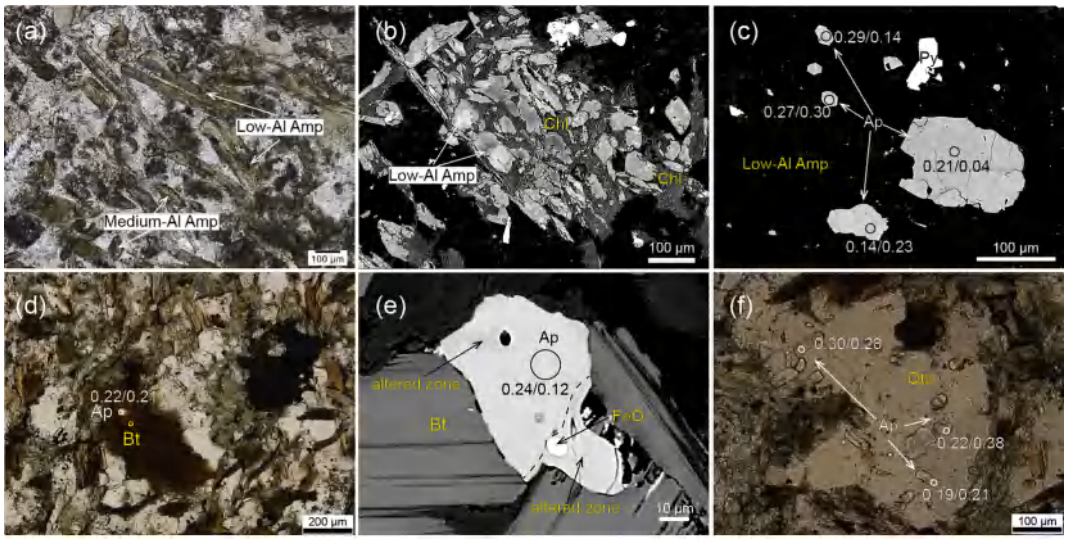

Fig. 7. Photomicrographs of apatite inclusions enclosed at igneous minerals in mafic microgranular enclaves. *(a)* elongated medium-Al and low-Al amphibole; *(b)* selective replacement of low-Al amphibole by chlorite aggregates; *(c)* irregular apatite inclusion in low-Al amphibole, coexisting with pyrite; *(d)* apatite-enclosed magmatic biotite with worn and uneven edges, showing features of captured phenocrysts; *(e)* irregular apatite in magmatic biotite, coexisting with iron oxide; *(f)* abundant apatite in the groundmass.

were analyzed using a JEOL JXA-8230 electron microprobe at the Shandong Analysis Center of China Metallurgical Geology Bureau (SDGB). The accelerating voltage was 15 kV for all the minerals, but the beam current was 10 nA for apatite and feldspar, 20 nA for amphibole and biotite. Apatite concentration profiles with 0.1-μm spacing were acquired using a focused beam. The on-peaking counting times of apatite were 60 s for F, Cl, and S, 30 s for Ce and Fe, 20 s for Na and Si, 10 s for the rests, while amphibole, biotite, and feldspar were 10 s for all the elements. If possible, apatite inclusions were analyzed with their c-axes not parallel to the direction of the electron beam, such that there should be a minimal extent of F migration during analysis (Goldoff et al., 2012). Relative errors are <1% for major elements in apatite (Ca and P),

< 2–3% for F and Cl, and <10% for minor elements (S, Si, Ce, Na, Mg).

24 apatite inclusions trace element analyses were also conducted at the SDGB, using a Coherent GeoLasPro 193 nm ArF Excimer laser ablation system connected to a Thermo Fisher ICAP Q. Ablation repetition rate was 6 Hz with a 40 μm beam aperture and 10 J cm^{-2} energy density. Trace element compositions were calibrated against various reference materials (NIST SRM 610, NIST SRM 612, BHVO-2G, BCR-2G, and BIR-1G), relative to an internal standard. Each analysis incorporated a background acquisition of approximately 25 s followed by 60 s of data acquisition from the sample. The Relative Standard Deviation of most elements (REE, U, Th, Pb) is <3%.

4.3. Calculation methods

4.3.1. Amphibole thermobarometer and oxygenbarometer

Amphibole has been widely used for constraining the magmatic temperatures and pressures (600–1100 °C and 0.1–25 kbar) (Ridolfi et al., 2010). Here the Si*-sensitive thermometer and the ΔNNO-Mg* equations (ΔNNO is the deviation of logfO_2 from the NNO buffer) of (Ridolfi et al., 2010) and Al-in amphibole geobarometer (Schmidt, 1992) were used to estimate *T*, *P*, and fO_2 of the magma from which amphibole crystallizes:

$$T\ (^{\circ}C) = (-151.487 \times Si^{*}) + 2041\ (\sigma est = \pm 22\ ^{\circ}C) \quad (1)$$

$$P(kbar) = -3.01 + (4.76 \times Al^{total}(\sigma est = \pm 0.6 kabr) \quad (2)$$

$$\Delta NNO = (1.644 \times Mg^{*}) - 4.01(\sigma est = \pm 0.22 logunit) \quad (3)$$

where $Si^{*} = Si + (Al^{IV}/15) - (2 \times Ti^{IV}) - (Al^{VI}/2) - (Ti^{VI}/1.8) + (Fe^{3+}/9) + (Fe^{2+}/3.3) + (Mg/26) + ({}^{B}Ca/5) + ({}^{B}Na/1.3) - ({}^{A}Na/15) + ((1 - {}^{A}Na - {}^{A}K)/2.3)$; $Mg^{*} = Mg + (Si/47) - (Al^{IV}/9) - (1.3 \times Ti^{VI}) + (Fe^{3+}/3.7) + (Fe^{2+}/5.2) - ({}^{B}Ca/20) - ({}^{A}Na/2.8) + ((1 - {}^{A}Na - {}^{A}K)/9.5)$. To eliminate errors arising from the use of different calculation methods, here we adopt the newly published Geo-fO2 software (Li et al., 2019a) to recalculate the experimental and collected amphibole data of the Pulang deposit.

4.3.2. Biotite thermobarometer and oxygenbarometer

The Ti-in-biotite geothermometer of (Henry et al., 2005) and ^{T}Al-geobarometer of (Uchida et al., 2007) are used to estimate *T-P* of the magma from which magmatic biotites crystallize:

$$T\ (^{\circ}C) = \left\{ \frac{\left[ln(Ti) + 2.3594 + 1.7283 \times (X_{Mg})^3 \right]}{4.6482 \times 10^{-9}} \right\}^{0.333} \quad (4)$$

$$P(kbar) = 3.03 \times T_{Al} - 6.53(\sigma est = \pm 0.33 kbar) \quad (5)$$

The Ti-in biotite empirical equation is strictly valid only for X_{Mg} = 0.275–1.000, Ti = 0.04–0.60 *apfu* and *T* = 480–800 °C. Estimations of the Ti-in-biotite geothermometer are ± 24 °C at temperatures of 480–600 °C, ± 23 °C at 600–700 °C, and ± 12 °C at 700–800 °C (Henry et al., 2005). All biotites analyzed here satisfy the above conditions (see details in Table).

Magmatic biotite can be used to estimate fO_2 through the following equilibrium reaction and Gibbs equilibrium constant (Wones and Eugster, 1965):

$KFe_3AlSi_3O_{10}(OH)_2$ (Biotite) + $0.5O_2$ = $KAlSi_3O_8$ (K-feldspar) + Fe_3O_4 (Magnetite) + H_2O

$$logfH2O = \left(\frac{7400}{T}\right) + 4.25 + 0.5 logfO_2 + 3logx - loga_{KAlSi3O8} - loga_{Fe3O4} \quad (6)$$

where x is the mole fraction of Fe^{2+} in the octahedral site of biotite, a represents activity, *fH2O* is calculated using the modified Redlich-Kwong equation (Holloway and Blank, 1994), $a_{KAlSi3O8}$ is calculated from the ternary feldspar model of (Elkins and Grove, 1990), $a_{Fe3O4} = (X_{mag})^2 \times \gamma_{mag}$, X_{mag}, and γ_{mag}, are estimated through (Carmichael, 1966) and (Woodland and Wood, 1994), respectively.

4.3.3. Using apatite to model melt Cl and S concentrations

To calculate the melt Cl and S concentrations, we need to know the equilibration temperature of apatite and melt. The empirical equation for calculating the apatite saturation temperature (AST) can be expressed as (Harrison and Watson, 1984):

$$\ln D_P^{apatite/melt} = \left(\frac{8400 + 26400 \times (SiO_2 - 0.5) \times 26400}{T}\right) - [3.1 + (12.4 \times (SiO_2 - 0.5))] \quad (7)$$

where $D_P^{apatite/melt}$ is the ratio of P concentration in apatite and melt, P_2O_5; SiO_2 is the weight fraction of the silica in the melt. T is the temperature in Kelvin.

Since the simple Nernst apatite/melt partition coefficients for Cl cannot be used to estimate the melt Cl concentration (Boyce et al., 2014), here we make use of the recently calibrated thermodynamic apatite/melt chlorine partitioning model of Li and Hermann (2017) using experiment data from Webster et al (2009) at 200 MPa and 900 °C. According to Li and Hermann (2017):

$$Cl_{melt}(wt\%) = \frac{X_{Cl}^{ap}}{X_{OH}^{ap}} \frac{1}{Kd_{Cl-OH}^{ap-melt}} \times 10.79 \quad (8)$$

where X_{Cl}^{ap} and X_{OH}^{ap} are the mole fractions of chlorapatite and hydroxylapatite, respectively, and

$$Kd_{Cl-OH}^{ap-melt} = e^{(25.81 + (X_{Cl}^{Ap} - X_{OH}^{Ap}) \times 17.33) \times \frac{10^3}{8.314 \times T}} \quad (9)$$

with the temperature (T) in Kelvin.

Considering that $D_S^{Ap-melt}$ ($D_S^{Ap-melt} = \frac{C_S^{Ap}}{C_S^{melt}}$; where C_S^{Ap} and C_S^{melt} represent the concentration of sulfur in apatite and the melt respectively) varies with apatite sulfur concentration, melt composition, and oxygen fugacity (Peng et al., 1997; Konecke et al., 2019), we calculate $D_S^{Ap-melt}$ values using equations determined for trachyandesite (Peng et al., 1997):

$$\ln D_S^{Ap-melt} = 21130/T - 16.2 \quad (10)$$

where T is in Kelvin.

5. Results

5.1. Amphibole, biotite and feldspar major element

All three types of amphibole from CQD, QMP, and MMEs are calcic amphiboles with $(Ca + Na)_B > 1.8$, and $Ca_B > 1.7$ (B represents two M4 sites per formula unit; Supplementary Table S1) according to the classification of Leake et al. (1997). Subdivision of these calcic amphiboles according to this system indicates that high-Al amphibole (Al_2O_3 = 8.56–12.02 wt%) comprises a tschermakite or Mg-amphibole, whereas medium-Al amphiboles (Al_2O_3 = 5.83–7.85 wt%) are all classified as Mg-amphibole (Fig. 8a). Additionally, variations in Al_{tot} of all these amphiboles are mostly attributed to the edenite exchange reaction, while the Al-tschermak substitution plays only a minimal role in these variations (Fig. 8b). Low-Al amphiboles generally have Al_2O_3 contents <4.4 wt% and Si > 7.3, and they are mainly plotted in the fields of actinolite (Fig. 8a), which are considered not to be truly magmatic but crystallize under subsolidus conditions or just altered medium-Al amphiboles in the presence of exsolved fluids (Chivas, 1982; Hendry et al., 1985). Further, the existence of medium-Al amphiboles altered to low-Al ones (Fig. 6b) further confirms the hydrothermal origin of these low-Al

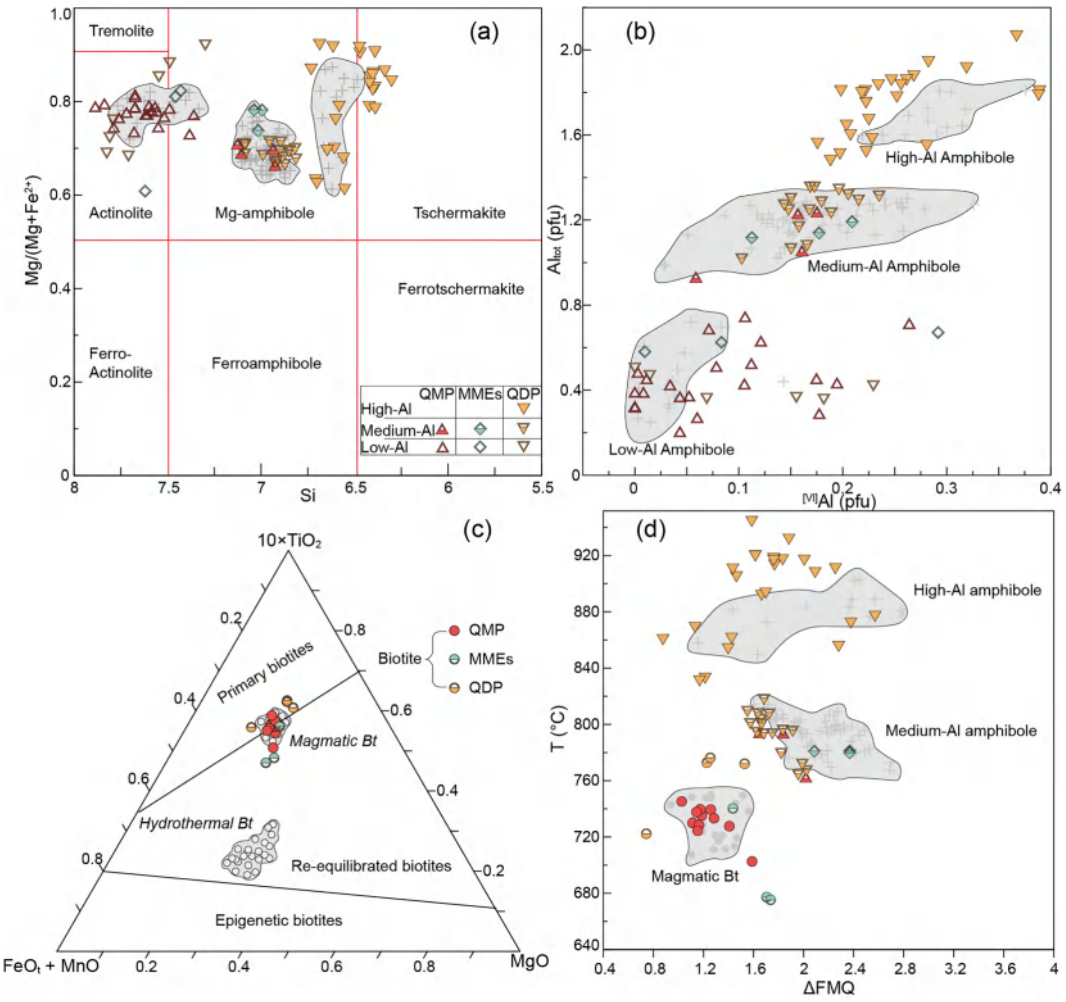

Fig. 8. *a* Classification of three types of amphiboles according to nomenclatures of (Leake et al., 1997); *b* Al-tschermak exchange in amphibole composition (Chelle-Michou and Chiaradia, 2017); *c* discrimination diagram of primary, re-equilibrated and epigenetic biotite (Nachit et al., 1985); *d* ΔFMQ versus temperature (T) diagram of amphibole and biotite. All published data for amphibole and biotite of the Pulang deposit are also shown as smaller white cross and circle (Data reSource: Cao et al., 2018; Leng et al., 2018; Li et al., 2019b).

amphiboles.

All the apatite-bearing biotites are magmatic Mg-biotites according to the classification of Foster (1960). The biotites in QMP and MMEs are almost located within the scope of previous studies, while those in CQD are slightly Ti-rich (Supplementary Table S2), indicating elevated crystallization temperatures (Fig. 8c). The calculated fO_2 (ΔFMQ) values of apatite-bearing biotites from both rock units display similar ranges of +0.7 to +1.6, consistent with the published data (Fig. 5d). The biotite crystallization temperatures and pressures of the QMP are 703–745 °C, 0.8–1.4 kbar, while those of the CQD and MMEs are 722–776 °C, 0.8–1.1 kbar, and 675–740 °C, 0.7–1.1 kbar, respectively (Fig. 8d).

The calculated temperatures, pressures, fO_2 (ΔFMQ) of high-Al amphiboles in CQD are 831–944 °C, 4.2–6.8 kbar, + 0.9 to + 2.6, respectively (Fig. 8d; Supplementary Table S1). Though the high-Al and medium-Al amphiboles have enclosed each other, the medium-Al amphiboles of CQD have lower calculated crystallization temperatures (764–818 °C) and pressures (1.8–3.4 kbar), but virtually identical fO_2 values (+1.6 to +2.0). Similarly, the calculated temperatures, pressures, and fO_2 (ΔFMQ) of the medium-Al amphiboles in QMP are 763–794 °C, 2.0–2.9 kbar, + 1.6 to + 2.0, respectively (Fig. 8d). Although the medium-Al amphiboles of MMEs are mostly elongated and show signatures of fast growth, they have almost identical crystallization temperatures (780–781 °C), pressures (2.3–2.7 kbar) and slightly higher fO_2 (ΔFMQ) values (+2.1 to +2.4; Fig. 8d).

As a result of the hydrothermal influence, the low-Al amphiboles of CQD, QMP, and MMEs have remarkably low temperatures (650–726 °C), but high fO_2 (ΔFMQ) values (+2.2 to +3.7; Fig. 8d). The calculated low pressures (which are mostly negative values) for these low-Al amphiboles also likely reflect the fact that they are hydrothermal-altered amphiboles from the medium- or high-Al amphiboles because the pressure limit for magmatic amphibole stability is 0.5 kbar as suggested by (Mutch et al., 2016). Therefore, the estimated P, T, and fO_2 values of these low-Al amphiboles have been discarded for discussion of magmatic evolution.

Apatite-bearing plagioclase phenocrysts in CQD and QMP range in composition from oligoclase to andesine (An = 13–46; Supplementary Table S3), with well-developed polysynthetic twinning.

5.2. Apatite major and halogen elements

Compositional distributions of S, F, and Cl in the primary, partly altered and extensively altered apatite have been documented in Fig. 9. The primary apatite grain of QMP is essentially homogeneous in terms of F and Cl contents even for those showing zoned BSE images, whereas the S content exhibit a clear multi-phase distribution pattern (Fig. 9a). Besides, the partly altered apatite reveals heterogeneous variability of S distribution (Fig. 9b), totally different from the S pattern of primary

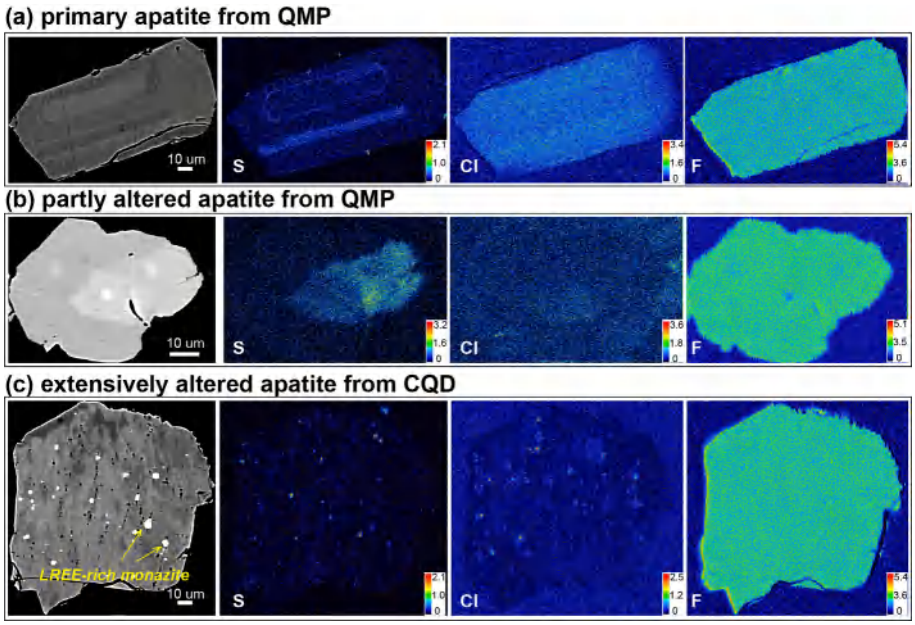

Fig. 9. Compositional distribution of S, Cl, and F in primary apatite *(a)* and partly altered apatite (b) from QMP and extensively altered apatite *(c)* from CQD, showing in X-ray maps from EPMA analyzes.

apatite, indicating a sufficient hydrothermal effect. Additionally, the F is homogeneously distributed and Cl exhibits features of slightly speckled distribution (Fig. 9b). Though the F content remains relatively steady, the S and Cl of the extensively altered apatite are mostly leached away, leaving only a few LREE-rich monazite spots (Fig. 9c). All the apatite grains are predominantly magmatic fluorapatite grains with variably Cl and SO_3 concentrations (Fig. 10; Supplementary Table S4). Although no systematic differences in Cl concentrations between apatite inclusions hosted in amphibole, plagioclase, and groundmass have been observed, the biotite-hosted apatites of QMP have broader and higher Cl contents (0.08–0.71 wt%) than others (Fig. 11a). On the contrary, the low-Al amphibole-hosted apatites of QMP usually have lower Cl contents (0.01–0.09 wt%, with one exception of 0.41 wt%). High-Al amphibole-enclosed apatite inclusions of CQD have lower Cl (0.03–0.04 wt%) than those (0.03–0.51 wt%) enclosed in medium-Al amphiboles or (0.03–0.13 wt%) low-Al amphiboles (Fig. 11a). The biotite-hosted apatite inclusions of CQD generally have lower Cl contents (0.09–0.21 wt%) than those of QMP. Since the apatite inclusions hosted in minerals of MMEs are likely captured phenocrysts from the porphyries, the F and Cl contents are similar to those of QMP. The acicular apatite inclusions in the groundmass of MMEs have normal Cl concentrations of 0.21 to 0.28 wt% (Fig. 11a).

Variations of apatite volatiles can typically be translated to X_F/X_{Cl} or X_{Cl}/X_{OH} ratios (Fig. 11b, c; where X_F, $X_{Cl,}$ and X_{OH} are the mole fractions of F, Cl, and OH, respectively). Unlike the published apatite grains of QMP, the biotite-hosted apatite inclusions have approximately constant X_F/X_{Cl} ratios (7.1–85.6) but broader X_{Cl}/X_{OH} ratios (0.11–1.41), especially compared with the low-Al amphibole-hosted ones (X_F/X_{Cl} = 12.3–964.3; X_{Cl}/X_{OH} = 0.02–0.28, respectively). Most apatite inclusions of CQD have more restricted X_F/X_{Cl} (8.0–266.1) and X_F/X_{OH} (1.8–13.6) ranges and fluctuating X_{Cl}/X_{OH} ratios (0.05–0.55), though some high-F contents cause negative X_{OH} values. Since the apatite inclusions of MMEs are mostly captured ones, their values are similar to those of QMP.

The most significant differences between the CQD, QMP, and MMEs are the S-rich apatites that are only observed from the biotite of QMP. Apart from the high and varying SO_3 concentrations (0.15–1.01 wt%) of biotite-hosted apatite inclusions of QMP, all the others hold low SO_3 values (<0.27 wt%) and fall in the range of published apatite grains values (Fig. 11d). Nonetheless, those apatite inclusions shielded in high-

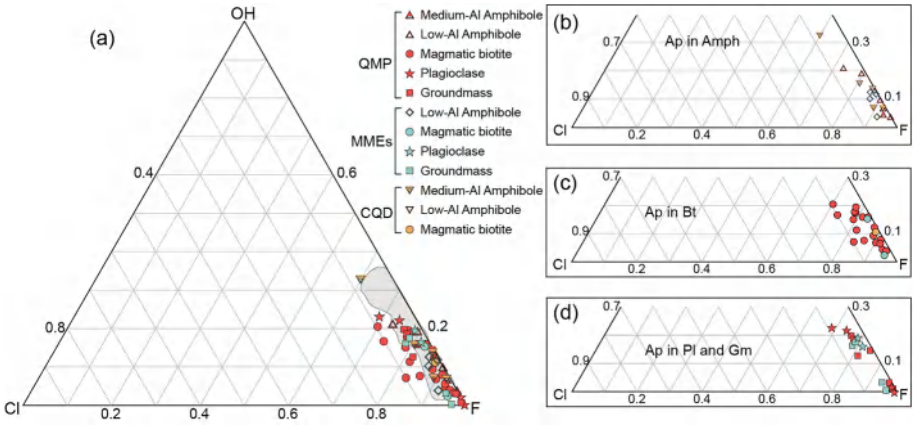

Fig. 10. F-OH-Cl ternary diagrams for apatite inclusions from the QMP, MMEs, and CQD *a*. Panels *b-d* show inclusions at different textural positions in different symbols.

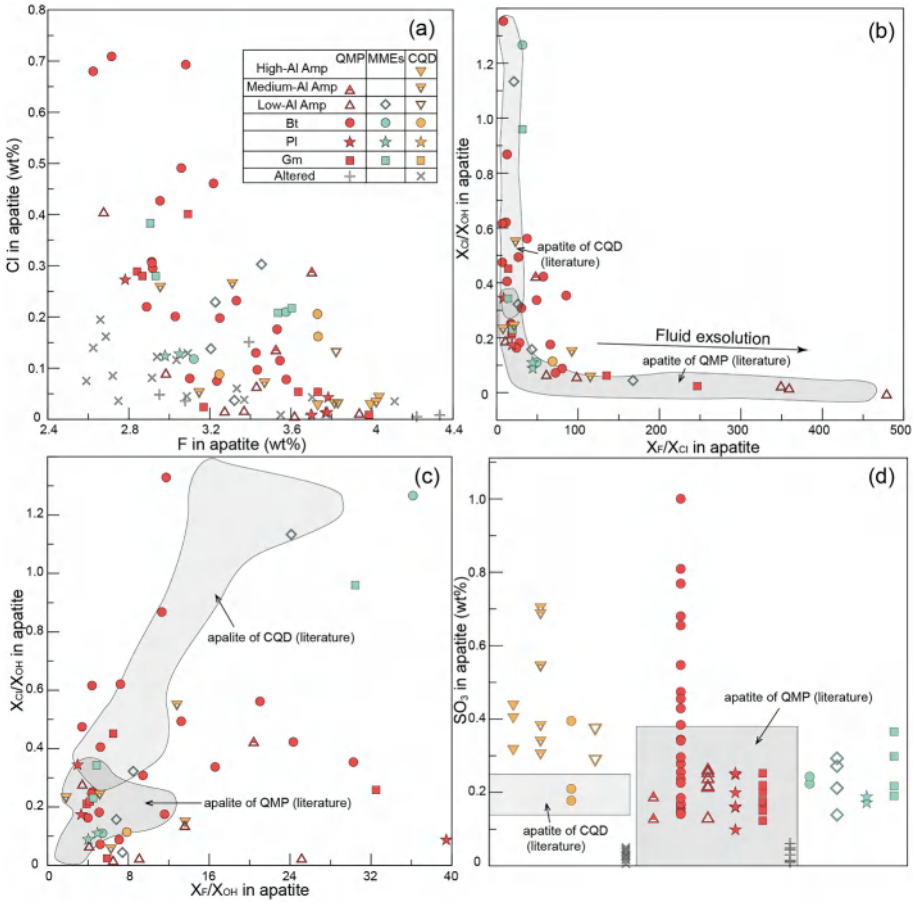

Fig. 11. Compositional changes in apatite volatile elements show crystals at different textural positions (Data source of published apatite: Pan et al., 2016, 2020; Xing et al., 2018, Gao et al., 2020).

Al and Medium-Al amphiboles of CQD have elevated SO_3 values (0.32–0.44; 0.30–0.70 wt%, respectively), compared with ones enclosed in low-Al amphibole and biotite (<0.40 wt%). Apatite inclusions of MMEs have normal SO_3 values (0.14–0.37 wt%), resembling those hosted in QMP (Fig. 11d).

All altered apatites from the CQD, QMP, and MMEs consistently have the lowest concentrations of Cl (0.01–0.22 wt%) and SO_3 (0.01–0.06 wt %), in comparison with the above magmatic apatites (Fig. 11d), indicating that these elements are depleted during the hydrothermal alteration (Bouzari et al., 2016). Since the initial compositions of magmatic apatite would be easily modified by the exsolved fluid via hydrothermal alteration, only those fluid inclusion-free, magmatic apatites that are used to evaluate the volatiles and trace element concentrations during magma evolution.

5.3. Apatite trace elements

Typically, apatite trace elements (Figs. 12, 13) exhibit differences not only in different host minerals (intra-rock) but also among different rock units (inter-rock). The biotite-, plagioclase- and groundmass-hosted apatites of QMP have relatively high Sr (785–1106 ppm, avg = 947 ppm, n = 11), Sr/Y ratios (2.21–3.62) and Mg (119–529 ppm with one exception of 9028 ppm, avg = 282 ppm, n = 10), but consistent low Y contents (220–373 ppm, avg = 326 ppm, n = 11), while those from the CQD and have much lower Sr (394–549 ppm, avg = 488 ppm, n = 10), Sr/Y ratios (0.82–0.97) and Mg (11–43 ppm with one exception hosted in biotite of 492 ppm, avg = 23 ppm, n = 9), but higher Y contents (508–796 ppm, avg = 651 ppm, n = 10; Fig. 12a, b, c). On the contrary, the low-Al amphibole-hosted apatite of QMP exhibit similar Sr (280–345 ppm, avg = 312 ppm, n = 2), Y (427–461 ppm, avg = 444 ppm, n = 2), Sr/Y ratios (0.61–0.81) and Mg (61–78 ppm, avg = 70 ppm, n = 2) values to the apatite from CQD (Fig. 12a, b, c). The apatites from QMP are characterized by higher Eu/Eu* values (0.55–0.73) than the ones from CQD (0.16–0.49), but all these apatites share similar Ce/Ce* values (Fig. 12d; 1.02–1.18). Although only one apatite inclusion from the MMEs has available trace element data, the value is similar to the apatite from CQD (Fig. 12).

All the apatite inclusions analyzed here are all enriched in light rare earth elements (LREE) and depleted in heavy rare earth elements (HREE) with negative Eu anomalies, slightly higher than those published apatite values (Fig. 13). Apatite total REE from the CQD (∑REE = 2750–10151 ppm, avg = 7023 ppm) and the MMEs (∑REE = 5352 ppm) exhibit higher values than those from the QMP (∑REE = 2561–6354 ppm, avg = 4646 ppm).

6. Discussion

6.1. Crystallization sequences and conditions of magmatic minerals and enclosed apatite inclusions

In the porphyries, apatite occurs as inclusions in all mineral phases and the groundmass and displays euhedral to subhedral habitus (Figs. 5, 6). This suggests that apatite crystallizes close to the liquidus in these porphyries. Assuming that the whole-rock chemistry approximates the compositions of the liquid at the time of apatite crystallization, the calculated AST is in the range of ~980 °C using the method of Harrison and Watson (1984). These temperatures are indeed close to the water-saturated liquidus of dacitic magmas in the upper crust (900–950 °C;

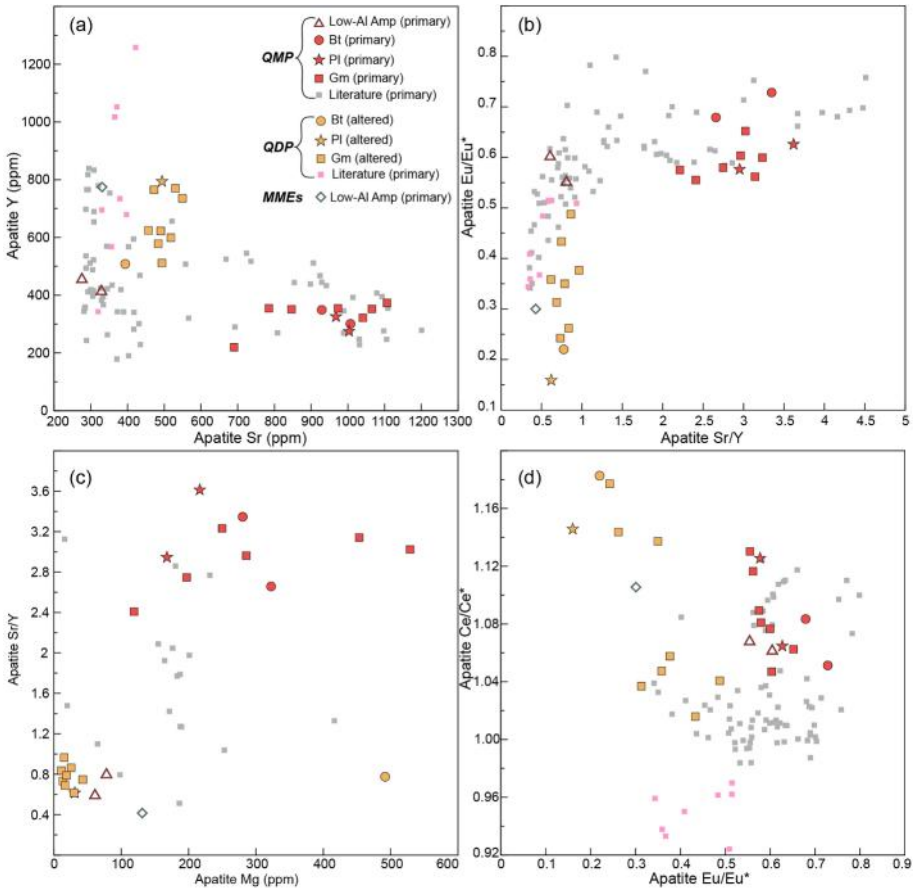

Fig. 12. Representative trace element compositions of apatite inclusions. Eu/Eu* is the europium anomaly, calculated as $Eu_N/(Sm_N \times Gd_N)^{0.5}$, using the chondrite normalization values of McDonough and Sun (1995). The chondrite values are also used in $Ce/Ce^* = Ce_N/(La_N \times Pr_N)^{0.5}$ (Data source of published apatite: Pan et al., 2016, 2020; Xing et al., 2018; Gao et al., 2020).

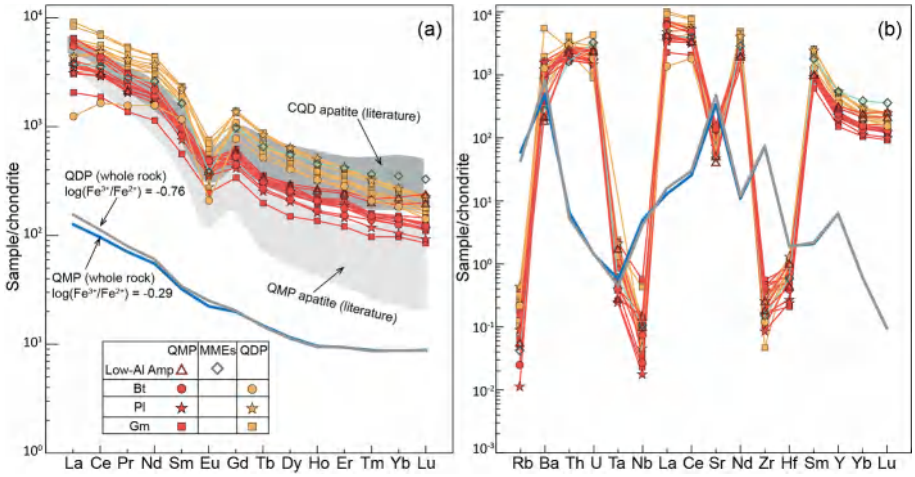

Fig. 13. Chondrite-normalized REE and trace element patterns of apatite inclusions from the QMP, MMEs, and CQD. Gray zones represent values of published apatite grains of the QMP and CQD at Pulang (Data source: Gao et al., 2020; Pan et al., 2020, 2016; Xing et al., 2018). The thick lines represent average values of the QMP and CQD (Data source: W.K. Li et al., 2019b). The C1 chondrite values are from McDonough and Sun (1995).

Costa et al., 2004). This is also similar to the highest crystallization temperature recorded by some apatite-enclosed high-Al amphiboles of CQD (~940 °C; Fig. 5a). Therefore, it is reasonable to conclude that the apatite inclusions in CQD and QMP could crystallize simultaneously and relatively early in the crystallization processes, with a possible temperature of 940–980 °C (Fig. 14).

In both CQD and QMP, crosscutting relationships of rock-forming minerals display similar crystallization sequences and conditions, which are, high-Al amphibole, medium-Al amphibole, magmatic biotite, plagioclase, low-Al amphibole (altered medium-Al amphibole), from early to late (Figs. 5, 6, 14). Such mineral crystallization sequences are also proved by the mineral thermometer using the existing empirical equation (Fig. 8d), where the calculated temperatures of medium-Al amphibole (~794 °C) are among the high-Al amphibole (~893 °C)

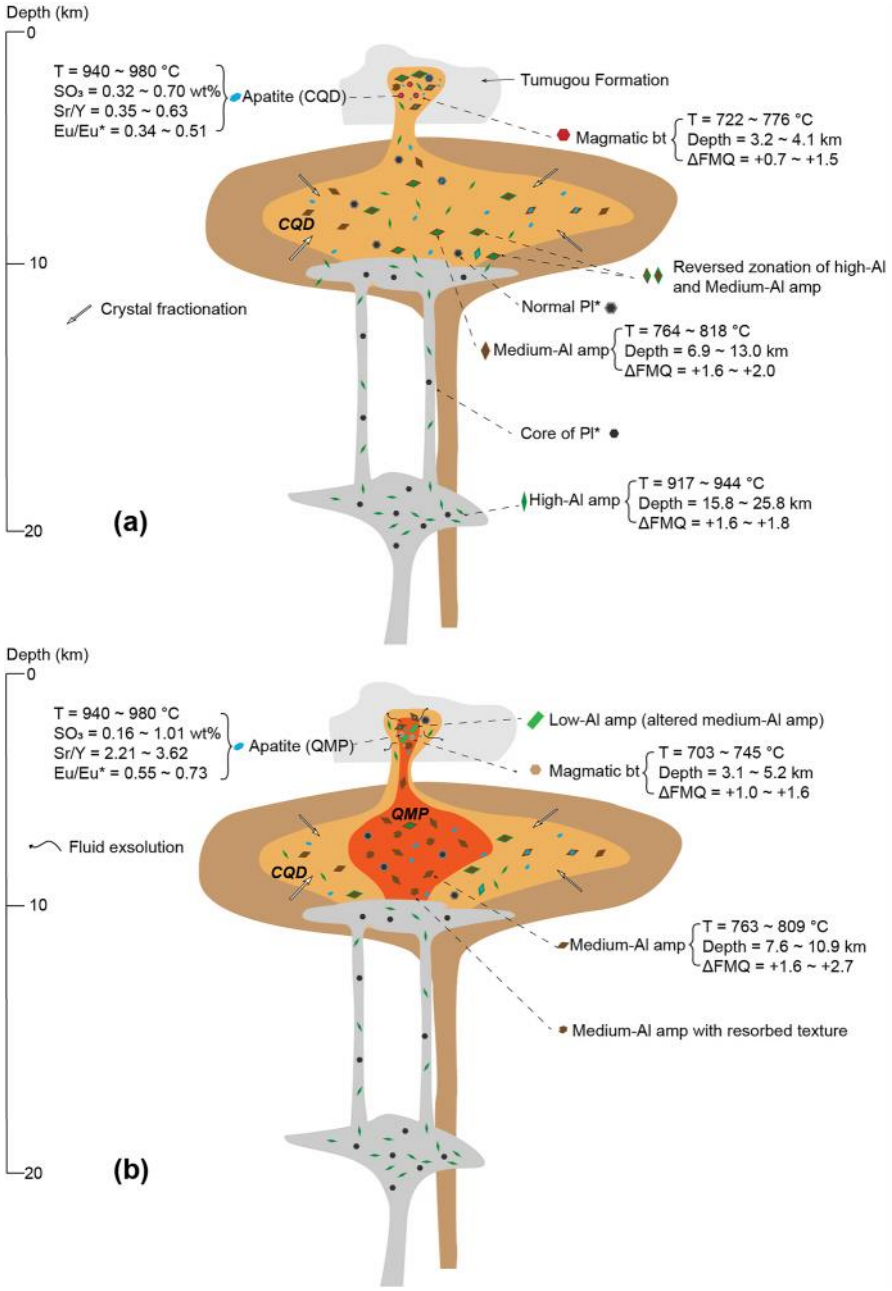

Fig. 14. Sketch for crystallization sequence of igneous minerals and variations of apatite inclusion at Pulang during upper crustal magma evolution (Minerals with an asterisk are from Li et al., 2019b). *(a)* Magma mixing occurred due to the injection of the relatively reduced (ΔFMQ = +1.6 ~ +1.8, calculated by high-Al amphibole) and LREE-enriched dioritic magma (Cao et al., 2009) from a deeper magma chamber (at ~20 km). This injection resulted in the reversed zonation of high-Al and medium-Al amphibole at ~10 km. Magmatic biotite crystallized as the mixed magma ascended and intruded the Tumugou formation (~4 km). The low Sr/Y and Eu/Eu* ratios of all enclosed apatites indicate a water-poor and reduced magma origin. *(b)* The prolonged injection of S-Cl enriched mafic magma introduced extensive magma mixing and possibly remelted the preexisting dioritic batholith and its interior apatites, and finally resulted in the abnormal S-Cl concentrations of biotite-hosted apatites with overgrowth texture, and triggered the magma degassing at the alteration of medium-Al amphiboles to low-Al amphiboles in the fertile QMP.

and magmatic biotite (~750 °C). Additionally, the presence of resorbed medium-Al amphibole and reversed compositional zones of high-Al and Medium-Al amphibole in CQD and QMP (Fig. 5d, 5e, 6a), both suggest that magma injection and mixing possibly occurred through multiple crystallization stages of medium-Al amphiboles at a depth of ~10 km (Fig. 14a, b). This is also consistent with the presence of elongated medium-Al amphibole and lack of high-Al amphibole in MMEs, which is the result of rapid cooling and magma mixing (Fig. 7a). Then magmatic biotite was crystallized at a paleodepth of ~4 km as the mixed magma further ascended and possibly intruded into the wall rocks (Tumugou Formation; Fig. 14a). Considering the rare presence of low-Al amphibole in barren CQD and abundance of such amphibole in fertile QMP, it is reasonable to conclude that only the fertile QMP has undergone extensive degassing and fluid exsolution processes, which have altered the medium-Al amphibole to low-Al amphibole and related mineralization (Fig. 14b).

Besides, magma mixing may also contribute to the fluctuation of magma fO_2 during upper crustal evolution. The initial magma of CQD and QMP displays very high fO_2 (ΔFMQ > + 3.0) as documented by zircon oxybarometer (Li et al., 2019b), decreasing to moderate fO_2 (ΔFMQ = + 1.6 to + 2.0) values as indicated medium-Al amphibole of both CQD and QMP. Such a decrease probably resulted from mixing with reduced magma as displayed by the high-Al amphibole with a broad fO_2 values (ΔFMQ = + 0.9 to + 2.6). The decrease of fO_2 values is also supported by the presence of primary sulfide inclusions in medium-Al amphibole (Fig. 5b). As the magma ascended and magmatic biotite crystallized, the fO_2 (ΔFMQ) values of magma further decrease to +0.7 ~ + 1.6). Such a fO_2 (ΔFMQ) decrease could be achieved by fractional crystallization, magma mixing, or contamination of wall rocks. Considering the shallow intrusion depth (~4 km) and late stage of magma evolution (~750 °C), the attenuated fractional crystallization process could not reduce the oxygen fugacity of CQD and therefore contamination of wall rocks could be highly possible. However, the QMP mostly intruded within CQD and had limited exposed area to wall rocks,

and it is hard to merely attribute the low fO_2 values of biotite in QMP to the contamination of wall rocks. Besides, we have noticed that the biotite-hosted apatite inclusions of QMP have distinctly different SO_3 patterns with overgrowth features (Fig. 9a) and show dramatically enriched SO_3 contents compared to all the other apatite inclusions (Fig. 11d). Therefore, the magma injection that occurred at the crystallization of medium-Al amphibole in CQD and QMP may last for a period of time and further provide a complement of excess sulfur (Fig. 14).

6.2. Sulfur and chlorine variations during magmatic-hydrothermal evolution

Experiments have shown that Cl and F is a fast-diffusive element (8×10^{-18} and 1×10^{-17} m^2/s at 900 °C, respectively), and preliminary results on S diffusivity at 800–900 °C also show values faster than those of Cl (Li et al., 2020a). This suggests that if volatiles have not been significantly exchanged with a surrounding phase (fluid, melt, or volatile-bearing mineral) after apatite inclusions enclosed in magmatic minerals, any initial volatiles zoning acquired during crystal growth should fade away and homogenize within weeks (Chelle-Michou and Chiaradia, 2017; Sato et al., 2017; Li et al., 2020a). As magmatic minerals (e.g., amphibole, biotite, plagioclase) start to crystallize, the apatite phenocrysts in equilibrium with the "present" melt are enclosed in these magmatic minerals and isolated from the evolving magma, thus the isolated apatite inclusions could preserve a record of melt compositions at the crystallization of igneous minerals.

The computed melt S concentrations of CQD are mainly between 594–821 ppm for high-Al amphibole-enclosed apatites, 571–1321 ppm for medium-Al amphibole-enclosed apatites, 335–744 ppm for biotite-hosted apatites (Fig. 15a, b, c, d). Besides, few scattered points from medium-Al hosted apatite domains result in higher apparent S melt concentrations and are discussed below. Going from the CQD to QMP, our data yield highly variable melt S contents for the biotite-hosted apatites of QMP, which even fall outside the range of arc basalts (probably within 300–1000 ppm; Fig. 15c). Similar S-rich apatites (SO_3 > 0.5 wt%) have also been reported in several natural systems, and their common association with anhydrite-saturated magmas suggests that they might have crystallized from abnormally S-enriched melts (Parat et al., 2011) or sulfur-fluxing events caused by a degassing underplated body of basalt (Van Hoose et al., 2013). The increasing of apatite SO_3 contents may either reflect (1) mafic melt injection (Chambefort et al., 2008; Van Hoose et al., 2013) or (2) increased melt S content with progressive fractional crystallization (Streck and Dilles, 1998) or (3) a temperature decreases during magma evolution (Peng et al., 1997; Scott et al., 2015) or (4) melting of preexisting lithologies and hosted apatite (Chelle-Michou and Chiaradia, 2017). Although the CQD and QMP have consistent mineral sequences and trace element patterns (Fig. 9), which are probably caused by similar fractional crystallization, the apatite in CQD systematically returns normal sulfur concentrations (Fig. 11d). Therefore, these distinctly different SO_3 contents could not be merely ascribed to the progressive fractional crystallization of melt. Besides, compared with the high-Al, medium-Al amphibole, and biotite-enclosed apatite, there are no systematically increased SO_3 contents of apatite. Thus, the decreased temperature could not be the reason for abnormal SO_3 contents of biotite-hosted apatite in QMP. The presence of S-rich apatite enclosed in biotite, and the overgrowth texture of apatite of QMP, together with the skeleton texture of some medium-Al amphiboles in QMP and CQD, both suggest that a possible magma mixing event may have occurred among the crystallization of medium-Al amphibole and magmatic biotite in QMP. Considering the widely distributed MMEs in the QMP, it is reasonable that the injection of sulfur-rich dioritic magma causes increasing SO_3 contents in biotite-hosted apatite of the ore-bearing QMP. Primary apatites in the MMEs are commonly acicular from fast growth due to undercooling, and they are not in equilibrium with their host melt, thus we could not obtain the related melt S contents (Fig. 7). Although the acicular apatite in the groundmass of MMEs has normal SO_3 contents, its abundance also seems to confirm an extra sulfur supplement process (Fig. 7f). However, whether the magma mixing caused the melting of preexisting CQD and hosted apatite could not be distinguished and need more work.

Chlorine is strongly partitioned into exsolved fluids in vapor-

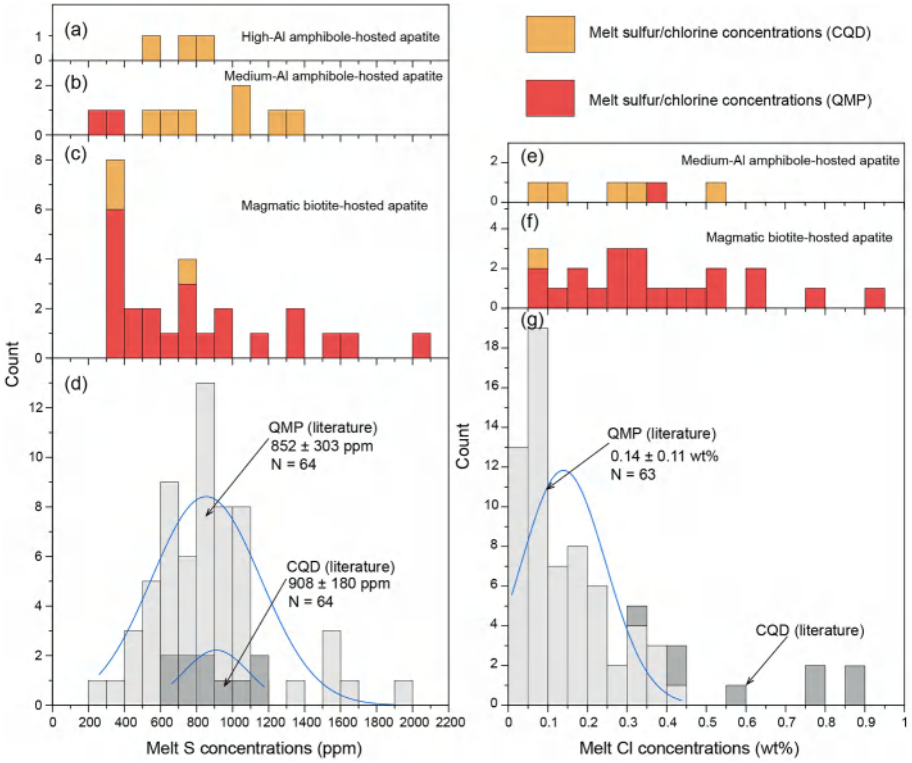

Fig. 15. Sulfur and chlorine concentrations of the melts that equilibrated with apatite from the QMP and CQD. *(a) (b) (c) (d)* melts S in equilibrium with high-Al amphibole-, medium-Al amphibole-, magmatic biotite-hosted apatite inclusions, and collected apatite grains (Data source: Pan et al., 2016, 2020; Xing et al., 2018; Gao et al., 2020); *(e) (f) (g)* melts Cl in equilibrium with high-Al amphibole-, magmatic biotite-hosted apatite inclusions, and collected apatite grains (Data source: Pan et al., 2016, 2020; Xing et al., 2018; Gao et al., 2020).

saturated magma, causing increased X_F/X_{Cl} and reduced X_{Cl}/X_{OH} ratios in residual melts (Masotta et al., 2016; Webster et al., 2009; Zajacz et al., 2012). However, the biotite-hosted apatite inclusions in QMP show relatively consistent X_F/X_{Cl} but elevated X_{Cl}/X_{OH} ratios, whereas the low-Al amphibole-hosted apatite exhibit high X_F/X_{Cl} and reduced X_{Cl}/X_{OH} ratios (Fig. 11d). Such variations could be ascribed to changes of volatile saturation states in magma evolution, for fluid-melt partition coefficients of Cl are typically high. These variations, together with the altered features of low-Al amphibole, both suggest that the magma initially was fluid undersaturated and became water saturated at the time of low-Al amphibole crystallization. Therefore, only those apatites crystallize in vapor-unsaturated conditions are used to calculate the melt Cl concentrations, including high-Al and medium-Al amphibole-hosted and magmatic biotite-hosted ones in CQD and QMP.

Estimates of melt chlorine concentration using apatite show a similar trend of melt sulfur concentration (Fig. 15e, f, g). It is worth noting that all calculated numbers are within the range of Cl melt concentrations of arc magmas (0.01–0.85 wt%; Aiuppa et al., 2009), even for those hosted in biotite of QMP (Fig. 15f). Overall, estimates based on biotite also record an increase in melt Cl concentrations. This increase confirms earlier thoughts that the injection of dioritic magma could account for the abnormal increase of sulfur and chlorine within biotite-enclosed apatite in QMP.

6.3. Using apatite trace elements as indicators of magmatic fertility

Apatite has recently been used as an indicator of magmatic fertility, especially in porphyry systems (Gao et al., 2020; Pan et al., 2020; Xing et al., 2020, 2021; Xu et al., 2021). Fractionation modeling of trace element conducted on apatite from the discrete stage of arc volcanic rocks have suggested that the notable trace element differences of apatite from different samples could be possibly explained by variable deep crustal fractionation, on the contrary, the differences of apatite that hosted in various minerals from the same sample are likely introduced by phenocrysts fractionation that co-crystallize with apatite in the shallow crust (Nathwani et al., 2020). As amphibole crystallizes first under a water-rich condition, whereas plagioclase crystallize crystallizes first under a water-poor condition (Loucks, 2014), Sr and Eu contents of apatite can be indicators of hydrous conditions of magma source. Additionally, apatite crystallizes from oxidized environments would have higher Eu but lower Ce than those from reduced environments, since increased Eu^{3+} and Ce^{3+} can substitute Ca^{2+} in apatite lattice (Sha and Chappell, 1999; Belousova et al., 2002). Therefore, a water-poor and reduced fO_2 condition for the CQD magma source, whereas a water-rich and oxidized magma source for the causative QMP can account for the differences of apatite trace elements from QMP and CQD (Fig. 12a, b). As the apatite inclusions of MMEs are mostly captured ones from its host porphyries, it is reasonable that it shows similar values to those in CQD (Fig. 12a, b). Experiments have shown that Mg in apatite is proportional to the Mg in the melt, suggesting that Mg in apatite can also be used as an indicator of magma differentiation (Prowatke and Klemme, 2006). Within our samples, the features that consistent Sr/Y_{ap} with decreasing Mg occurs in the apatite of QMP, except for those hosted in low-Al amphibole, indicate that the Sr/Y ratios of apatite do not vary significantly with changing melt composition (Fig. 12c). Whereas, no variations occur both in the Sr/Y_{ap} and Mg content of most altered apatite inclusions in the CQD, except for a single apatite hosted in biotite (which could have been contaminated by its surrounding Mg-biotite; Fig. 12c). Meanwhile, the low-Al amphibole-hosted apatite of QMP show sharply decreased Sr but solid Y contents and caused low Sr/Y ratios, similar to values of both altered and primary apatites in CQD (Fig. 12a, b). Considering the low-Al amphiboles are mostly altered medium-Al amphibole, it is reasonable to conclude that the hydrothermal fluids can easily extract Sr, even for those apatites with little characteristics of hydrothermal influence. This result may also account for the diverse Sr/Y ratios of primary apatite in QMP from previous studies. Therefore, using apatite Sr/Y ratios to discriminate magma adakitic affinities should be with cautions.

As mentioned above, the magma source is reduced fO_2 condition for CQD and oxidized fO_2 condition for QMP. This is consistent with the primary apatite Eu/Eu* ratios of CQD and QMP. However, the altered apatites of CQD have increased Ce/Ce* ratios, even higher than those in QMP. Combined with the widely distributed LREE-rich points in highly-altered apatite of CQD, the hydrothermal fluids may lead to a sharp increase in LREE concentrations of altered apatites and could account for the abnormally high Ce/Ce* ratios of the barren CQD. Using apatite Ce/Ce* ratios to discriminate magma fO_2 condition should be with cautions.

Therefore, we suggest that apatite Sr and LREE can be easily modified by hydrothermal fluids or evolving melts. Using apatite trace elements as efficient indicators in helping to properly interpret petrogenetic studies would be more robust for those apatites enclosed in primary magmatic minerals and isolated from the evolving magma or fluids.

6.4. Implications for the formation of porphyry deposits

Porphyry Cu deposits are formed by fluids released from felsic magmatic intrusions of batholithic dimensions, which are inferred to have been incrementally built up by a series of sill injections (Korges et al., 2020). However, this model then extends the problem that a single, copper-rich magmatic fluid could trigger both copper enrichment and the subsequent precipitation of sulfide ore minerals within a zone of hydrothermally altered rock. Of course, some hypotheses, including (1) abrupt changes of intensive parameters such as temperature, pressure (Landtwing et al., 2005; Proffett, 2009; Sillitoe, 2010); (2) mafic S-rich magma injection (Hattori and Keith, 2001; Caricchi et al., 2014; He et al., 2016); (3) injection of S-rich gas from the underlying mafic magma (Blundy et al., 2015); (4) anhydrite dissolution in the late-stage exsolved fluid (Streck and Dilles, 1998; Li et al., 2020c) have been proposed to convert the already-stabilized magmatic-hydrothermal system and cause the deposition of Cu. Here, the variations of volatiles in biotite-hosted apatite inclusions with overgrowth texture, and the occasionally observed medium-Al amphibole with skeleton texture of the fertile QMP at Pulang indicate that a series of sill injections of S-rich dioritic magma likely contribute to the sulfur enrichment among the crystallization of medium-Al amphiboles and magmatic biotites, and the subsequent remelting the preexisting dioritic batholith and its interior apatites, and finally trigger the magma degassing at the alteration of medium-Al amphiboles to low-Al amphiboles in the fertile QMP.

7. Conclusion

The combination of igneous minerals and enclosed apatite inclusions geochemistry in this study provides insights into the volatile evolutions and trace element behaviors during magma mixing and degassing processes. Combined with evidence for reverse zonation in high-Al and medium-Al amphibole phenocrysts in the barren CQD, and resorbed medium-Al amphiboles in the fertile QMP, the abnormal S-Cl enrichment of biotite-hosted apatite inclusions with overgrowth texture in QMP are possibly the results of periodical injections of a series of S-Cl rich mafic magma among the crystallization of medium-Al amphibole and magmatic biotite. The periodical recharge processes could account for the enormous metal endowment of giant porphyry deposits and have triggered ore formation by causing voluminous exsolution of metalliferous hydrothermal fluids. Additionally, for apatite, their Sr/Y ratios could be used to constrain magma H_2O content and Eu/Eu* ratios could be used in evaluating magma oxidation state, however, cautions should be taken when using the Ce/Ce* ratios in quantifying magma redox state for the high mobility of hydrothermal alteration.

Declaration of Competing Interest

The authors declare that they have no known competing financial interests or personal relationships that could have appeared to influence the work reported in this paper.

Acknowledgments

We would like to thank the editor and two anonymous reviewers for their constructive comments which have significantly improved the manuscript. We greatly appreciate Dr. Weiran Li (Nanyang Technological University, Singapore) for generously providing the "ApThermo" excel spreadsheet and advice for apatite analysis. We thank Tengda Guo, Shuang Xu, and Peijun Lin (SDGB) for assistance in EMPA analysis, Qingyu Gu, and Jilin Wang (SDGB) for help with LA-ICP-MS trace element analysis. This work is financially supported by the Nation Key Research and Development Program of China (Grant No. 2019YFA0708603), the 111 Project of the Ministry of Science and Technology, China (Grant No. BP0719021), and the MOST Special Fund from the State Key Laboratory of Geological Processes and Mineral Resources, China University of Geoscience (Grant No. MSFGPMR201804).

Appendix A. Supplementary data

Supplementary data to this article can be found online at https://doi.org/10.1016/j.oregeorev.2021.104509.

References

Aiuppa, A., Baker, D.R., Webster, J.D., 2009. Halogens in volcanic systems. Chem. Geol., Halogens in Volcanic Systems and Their Environmental Impacts 263, 1–18. https://doi.org/10.1016/j.chemgeo.2008.10.005.

Belousova, E.A., Griffin, W.L., O'Reilly, S.Y., Fisher, N.I., 2002. Apatite as an indicator mineral for mineral exploration: trace-element compositions and their relationship to host rock type. J. Geochem. Explor. 76 (1), 45–69. https://doi.org/10.1016/S0375-6742(02)00204-2.

Blundy, J., Mavrogenes, J., Tattitch, B., Sparks, S., Gilmer, A., 2015. Generation of porphyry copper deposits by gas–brine reaction in volcanic arcs. Nat. Geosci. 8 (3), 235–240. https://doi.org/10.1038/ngeo2351.

Bruand, E., Fowler, M., Storey, C., Darling, J., 2017. Apatite trace element and isotope applications to petrogenesis and provenance. Am. Mineral. 102 (1), 75–84. https://doi.org/10.2138/am-2017-5744.

Bouzari, F., Hart, C.J.R., Bissig, T., Barker, S., 2016. Hydrothermal alteration revealed by apatite luminescence and chemistry: a potential indicator mineral for exploring covered porphyry copper deposits. Econ. Geol. 111 (6), 1397–1410. https://doi.org/10.2113/econgeo.111.6.1397.

Boyce, J.W., Tomlinson, S.M., McCubbin, F.M., Greenwood, J.P., Treiman, A.H., 2014. The lunar apatite paradox. Science 344 (6182), 400–402. https://doi.org/10.1126/science:1250398.

Cao, D.H., Wang, A.J., Li, W.C., Wang, G.S., Li, R.P., Li, Y.K., 2009. Magma mixing in the Pulang porphyry copper deposit: evidence from petrology and element geochemistry. Acta Geol. Sin. 83, 166–175 (in Chinese with English abstract).

Cao, K., Xu, J.F., Chen, J.L., Huang, X.X., Ren, J.B., Zhao, X.D., Liu, Z.X., 2016. Double-layer structure of the crust beneath the Zhongdian arc, SW China: U-Pb geochronology and Hf isotope evidence. J. Asian Earth Sci. 115, 455–467. https://doi.org/10.1016/j.jseaes.2015.10.024.

Cao, K., Yang, Z.M., Xu, J.F., Fu, B., Li, W.K., Sun, M.Y., 2018. Origin of dioritic magma and its contribution to porphyry Cu-Au mineralization at Pulang in the Yidun arc, eastern Tibet. Lithos 304, 436–449. https://doi.org/10.1016/j.lithos.2018.02.018.

Cao, K., Li, W.K., Yang, Z.M., Mavrogenes, J., White, N.C., Xu, J.F., Li, Y., 2019. Geology and Genesis of the Giant Pulang Porphyry Cu-Au District, Yunnan, Southwest China. Econ. Geol. 114, 275–301. https://doi.org/10.5382/econgeo.2019.4631.

Caricchi, L., Annen, C., Blundy, J., Simpson, G., Pinel, V., 2014. Frequency and magnitude of volcanic eruptions controlled by magma injection and buoyancy. Nat. Geosci. 7 (2), 126–130. https://doi.org/10.1038/ngeo2041.

Carmichael, I.S.E., 1966. The iron-titanium oxides of salic volcanic rocks and their associated ferromagnesian silicates. Contr. Mineral. Petrol. 14 (1), 36–64. https://doi.org/10.1007/BF00370985.

Chambefort, I., Dilles, J.H., Kent, A.J.R., 2008. Anhydrite-bearing andesite and dacite as a source for sulfur in magmatic-hydrothermal mineral deposits. Geology 36 (9), 719. https://doi.org/10.1130/G24920A.110.1130/2008181.

Chelle-Michou, C., Chiaradia, M., 2017. Amphibole and apatite insights into the evolution and mass balance of Cl and S in magmas associated with porphyry copper deposits. Contrib. Mineral. Petrol. 172, 105. https://doi.org/10.1007/s00410-017-1417-2.

Chivas, A.R., 1982. Geochemical evidence for magmatic fluids in porphyry copper mineralization. Contrib. Mineral. Petrol. 78 (4), 389–403. https://doi.org/10.1007/BF00375201.

Costa, F., Scaillet, B., Pichavant, M., 2004. Petrological and experimental constraints on the pre-eruption conditions of Holocene dacite from Volcán San Pedro (36 S, Chilean Andes) and the importance of sulphur in silicic subduction-related magmas. J. Petrol. 45, 855–881. https://doi.org/10.1093/petrology/egg114.

Deng, J., Wang, Q., Li, G., Li, C., Wang, C., 2014a. Tethys tectonic evolution and its bearing on the distribution of important mineral deposits in the Sanjiang region, SW China. Gondwana Res. 26 (2), 419–437. https://doi.org/10.1016/j.gr.2013.08.002.

Deng, J., Wang, Q.F., Li, G.J., Santosh, M., 2014b. Cenozoic tectono-magmatic and metallogenic processes in the Sanjiang region, southwestern China. Earth-Sci. Rev. 138, 268–299. https://doi.org/10.1016/j.earscirev.2014.05.015.

Elkins, L.T., Grove, T.L., 1990. Ternary feldspar experiments and thermodynamic models. Am. Mineral. 75, 544–559.

Fan, Y.H., Li, W.C., 2006. Geological characteristics of the Pulang porphyry copper deposit, Yunnan. Geol. China (in Chinese with English abstract).

Foster, M.D., 1960. Interpretation of the composition of trioctahedral micas. US Geol. Surv. Prof. Pap., B 354, 1–49.

Gao, X., Yang, L.Q., Wang, C.G., He, W.Y., Bao, X.S., Zhang, S.Y., 2020. Halogens and trace elements of apatite from Late Mesozoic and Cenozoic porphyry Cu-Mo-Au deposits in SE Tibet, China: constraints on magmatic fertility and granitoid petrogenesis. J. Asian Earth Sci. 203, 104552. https://doi.org/10.1016/j.jseaes.2020.104552.

Goldoff, B., Webster, J.D., Harlov, D.E., 2012. Characterization of fluor-chlorapatites by electron probe microanalysis with a focus on time-dependent intensity variation of halogens. Am. Mineral. 97 (7), 1103–1115. https://doi.org/10.2138/am.2012.3812.

Harrison, T.M., Watson, E.B., 1984. The behavior of apatite during crustal anatexis: equilibrium and kinetic considerations. Geochim. Cosmochim. Acta 48 (7), 1467–1477. https://doi.org/10.1016/0016-7037(84)90403-4.

Hattori, K.H., Keith, J.D., 2001. Contribution of mafic melt to porphyry copper mineralization: evidence from Mount Pinatubo, Philippines, and Bingham Canyon, Utah, USA. Miner. Deposita 36 (8), 799–806. https://doi.org/10.1007/s001260100209.

He, W.Y., Mo, X.X., Yang, L.Q., Xing, Y.L., Dong, G.C., Yang, Z., Gao, X., Bao, X.S., 2016. Origin of the Eocene porphyries and mafic microgranular enclaves from the Beiya porphyry Au polymetallic deposit, western Yunnan, China: implications for magma mixing/mingling and mineralization. Gondwana Res. 40, 230–248. https://doi.org/10.1016/j.gr.2016.09.004.

Hedenquist, J.W., Lowenstern, J.B., 1994. The role of magmas in the formation of hydrothermal ore deposits. Nature 370 (6490), 519–527. https://doi.org/10.1038/370519a0.

Hendry, D.A.F., Chivas, A.R., Long, J.V.P., Reed, S.J.B., 1985. Chemical differences between minerals from mineralizing and barren intrusions from some North American porphyry copper deposits. Contrib. Mineral. Petrol. 89 (4), 317–329. https://doi.org/10.1007/BF00381554.

Henry, D.J., Guidotti, C.V., Thomson, J.A., 2005. The Ti-saturation surface for low-to-medium pressure metapelitic biotites: implications for geothermometry and Ti-substitution mechanisms. Am. Mineral. 90, 316–328. https://doi.org/10.2138/am.2005.1498.

Holloway, J.R., Blank, J.G., 1994. Application of experimental results to COH species in natural melts. Rev. Mineral. 30, 187–187. https://doi.org/10.1515/9781501509674-012.

Hou, Z.Q., Mo, X., Tan, J., Hu, S., Luo, Z., 1993. The eruption sequences of basalts in the Yidun island arc, Sanjiang region and evolution of rift to island arc. Bull. Chin. Acad. Geol. Sci. 26, 49–67 (in Chinese).

Hou, Z.Q, Zaw, K., Pan, G.T., Mo, X.X., Xu, Q., Hu, Y.Z., Li, X.Z., 2007. Sanjiang Tethyan metallogenesis in SW China: tectonic setting, metallogenic epochs and deposit types. Ore Geol. Rev. 31 (1–4), 48–87. https://doi.org/10.1016/j.oregeorev.2004.12.007.

Hou, Z.Q., Yang, Y.Q., Wang, H.P., Qu, X.M., Lü, Q.T., Huang, D.H., Wu, X.Z., Yu, J.J., Tang, S.H., Zhao, J.H., 2003. The Collisional Orogeny and Mineralization Systems of the Yidun Arc Orogen in Sanjiang Region, China. Geological Publishing House, Beijing, pp. 154–187 (in Chinese with English abstract).

Hughes, J.M., Rakovan, J., 2002. The crystal structure of apatite, Ca5 (PO4) 3 (F, OH, Cl). Rev. Mineral. Geochem. 48 (1), 1–12. https://doi.org/10.2138/rmg.2002.48.1.

Jennings, E.S., Marschall, H.R., Hawkesworth, C.J., Storey, C.D., 2011. Characterization of magma from inclusions in zircon: apatite and biotite work well, feldspar less so. Geology 39, 863–866. https://doi.org/10.1130/G32037.1.

Konecke, B.A., Fiege, A., Simon, A.C., Linsler, S., Holtz, F., 2019. An experimental calibration of a sulfur-in-apatite oxybarometer for mafic systems. Geochim. Cosmochim. Acta 265, 242–258. https://doi.org/10.1016/j.gca.2019.08.044.

Korges, M., Weis, P., Andersen, C., 2020. The role of incremental magma chamber growth on ore formation in porphyry copper systems. Earth Planet. Sci. Lett. 552, 116584. https://doi.org/10.1016/j.epsl.2020.116584.

Landtwing, M., Pettke, T., Halter, W., Heinrich, C., Redmond, P., Einaudi, M., Kunze, K., 2005. Copper deposition during quartz dissolution by cooling magmatic–hydrothermal fluids: the Bingham porphyry. Earth Planet. Sci. Lett. 235 (1-2), 229–243. https://doi.org/10.1016/j.epsl.2005.02.046.

Leake, B.E., Woolley, A.R., Arps, C.E., Birch, W.D., Gilbert, M.C., Grice, J.D., Hawthorne, F.C., Kato, A., Kisch, H.J., Krivovichev, V.G., 1997. Nomenclature of amphiboles; report of the subcommittee on amphiboles of the International Mineralogical Association, Commission on New Minerals and Mineral Names. Can. Mineral. 35, 219–246.

Leng, C.B., Zhang, X.C., Hu, R.Z., Wang, S.X., Zhong, H., Wang, W.Q., Bi, X.W., 2012. Zircon U-Pb and molybdenite Re–Os geochronology and Sr–Nd–Pb–Hf isotopic constraints on the genesis of the Xuejiping porphyry copper deposit in Zhongdian,

Northwest Yunnan, China. J. Asian Earth Sci. 60, 31–48. https://doi.org/10.1016/j.jseaes.2012.07.019.
Leng, C.B., Huang, Q.Y., Zhang, X.C., Wang, S.X., Zhong, H., Hu, R.Z., Bi, X.W., Zhu, J.J., Wang, X.S., 2014. Petrogenesis of the Late Triassic volcanic rocks in the Southern Yidun arc, SW China: constraints from the geochronology, geochemistry, and Sr–Nd–Pb–Hf isotopes. Lithos 190, 363–382. https://doi.org/10.1016/j.lithos.2013.12.018.
Leng, C.B., Gao, J.F., Chen, W.T., Zhang, X.C., Tian, Z.D., Guo, J.H., 2018. Platinum-group elements, zircon Hf-O isotopes, and mineralogical constraints on magmatic evolution of the Pulang porphyry Cu-Au system, SW China. Gondwana Res. https://doi.org/10.1016/j.gr.2018.03.001.
Li, H.J., Hermann, J., 2017. Chlorine and fluorine partitioning between apatite and sediment melt at 2.5 GPa, 800℃: A new experimentally derived thermodynamic model. Am. Mineral. 102, 580–594. https://doi.org/10.2138/am-2017-5891.
Li, J.X., Li, G.M., Evans, N.J., Zhao, J.X., Qin, K.Z., Xie, J., 2020c. Primary fluid exsolution in porphyry copper systems: evidence from magmatic apatite and anhydrite inclusions in zircon. Miner. Deposita 56 (2), 407–415. https://doi.org/10.1007/s00126-020-01013-4.
Li, W.C., Yu, H.J., Gao, X., Liu, X.L., Wang, J.H., 2017. Review of Mesozoic multiple magmatism and porphyry Cu–Mo (W) mineralization in the Yidun Arc, eastern Tibet Plateau. Ore Geol. Rev. 90, 795–812. https://doi.org/10.1016/j.oregeorev.2017.03.009.
Li, W.R., Chakraborty, S., Nagashima, K., Costa, F., 2020a. Multicomponent diffusion of F, Cl and OH in apatite with application to magma ascent rates. Earth Planet. Sci. Lett. 550, 116545. https://doi.org/10.1016/j.epsl.2020.116545.
Li, W.R., Costa, F., Nagashima, K., 2020b. Apatite crystals reveal melt volatile budgets and magma storage depths at Merapi volcano, Indonesia. J. Petrol. https://doi.org/10.1093/petrology/egaa100.
Li, W.K., Cheng, Y.Q., Yang, Z.M., 2019a. Geo-fO2: Integrated Software for Analysis of Magmatic Oxygen Fugacity. Geochem. Geophys. Geosystems 20, 2542–2555.https://doi.org/10.1029/2019GC008273.
Li, W.K., Yang, Z.M., Cao, K., Lu, Y., Sun, M.Y., 2019b. Redox-controlled generation of the giant porphyry Cu–Au deposit at Pulang, southwest China. Contrib. Mineral. Petrol. 174, 12. https://doi.org/10.1007/s00410-019-1546-x.
Li, W.C., Zeng, P.S., Hou, Z.Q., Noel, C.W., 2011. The Pulang porphyry copper deposit and associated felsic intrusions in Yunnan Province, Southwest China. Econ. Geol. 106 (1), 79–92. https://doi.org/10.2113/econgeo.106.1.79.
Liu, H., Zhang, C.Q., Jia, F.D., Zhou, Y.M., Lou, D.B., 2015. Mineral and geochemical evidences of magma-mixing from Pulang porphyry copper deposit in SW Sanjiang, China. Acta Petrol. Sin. 31, 3189–3202 (in Chinese with English abstract).
Lloyd, A.S., Plank, T., Ruprecht, P., Hauri, E.H., Rose, W., 2013. Volatile loss from melt inclusions in pyroclasts of differing sizes. Contrib Mineral Petrol 165 (1), 129–153. https://doi.org/10.1007/s00410-012-0800-2.
Loucks, R.R., 2014. Distinctive composition of copper-ore-forming arcmagmas. Aust. J. Earth Sci. 61 (1), 5–16. https://doi.org/10.1080/08120099.2013.865676.
Mao, M., Rukhlov, A.S., Rowins, S.M., Spence, J., Coogan, L.A., 2016. Apatite trace element compositions: a robust new tool for mineral exploration. Econ. Geol. 111 (5), 1187–1222. https://doi.org/10.2113/econgeo.111.5.1187.
Masotta, M., Keppler, H., Chaudhari, A., 2016. Fluid-melt partitioning of sulfur in differentiated arc magmas and the sulfur yield of explosive volcanic eruptions. Geochim. Cosmochim. Acta 176, 26–43. https://doi.org/10.1016/j.gca.2015.12.014.
Maughan, D., Keith, J., Christiansen, E., Pulsipher, T., Hattori, K., Evans, N., 2002. Contributions from mafic alkaline magmas to the Bingham porphyry Cu–Au–Mo deposit, Utah, USA. Miner. Deposita 37 (1), 14–37. https://doi.org/10.1007/s00126-001-0228-5.
McCubbin, F.M., Jones, R.H., 2015. Extraterrestrial apatite: planetary geochemistry to astrobiology. Elements 11 (3), 183–188. https://doi.org/10.2113/gselements.11.3.183.
McDonough, W.F., Sun, S.S., 1995. The composition of the Earth. Chem. Geol. 120 (3–4), 223–253. https://doi.org/10.1016/0009-2541(94)00140-4.
Mutch, E.J.F., Blundy, J.D., Tattitch, B.C., Cooper, F.J., Brooker, R.A., 2016. An experimental study of amphibole stability in low-pressure granitic magmas and a revised Al-in-hornblende geobarometer. Contrib. Mineral. Petrol. 171, 85. https://doi.org/10.1007/s00410-016-1298-9.
Nachit, H., Razafimahefa, N., Stussi, J.-M., Carron, J.-P., 1985. Composition chimique des biotites et typologie magmatique des granitoides. Comptes rendus de l'Académie des sciences. Série 2, Mécanique, Physique, Chimie, Sciences de l'univers, Sciences de la Terre 301, 813–818.
Nathwani, C.L., Loader, M.A., Wilkinson, J.J., Buret, Y., Sievwright, R.H., Hollings, P., 2020. Multi-stage arc magma evolution recorded by apatite in volcanic rocks. Geology 48, 323–327. https://doi.org/10.1130/G46998.1.
Pan, L.C., Hu, R.Z., Wang, X.S., Bi, X.W., Zhu, J.J., Li, C., 2016. Apatite trace element and halogen compositions as petrogenetic-metallogenic indicators: examples from four granite plutons in the Sanjiang region, SW China. Lithos 254–255, 118–130. https://doi.org/10.1016/j.lithos.2016.03.010.
Pan, L.C., Hu, R.Z., Bi, X.W., Wang, Y., Yan, J., 2020. Evaluating magmatic fertility of Paleo-Tethyan granitoids in northeastern Tibet using apatite chemical composition and Nd isotope. Ore Geol. Rev. 103757 https://doi.org/10.1016/j.oregeorev.2020.103757.
Pan, Y., Fleet, M.E., 2002. Compositions of the apatite-group minerals: substitution mechanisms and controlling factors. Rev. Mineral. Geochem. 48 (1), 13–49. https://doi.org/10.2138/rmg.2002.48.2.
Parat, F., Holtz, F., Klügel, A., 2011. S-rich apatite-hosted glass inclusions in xenoliths from La Palma: constraints on the volatile partitioning in evolved alkaline magmas. Contrib. Mineral. Petrol. 162 (3), 463–478. https://doi.org/10.1007/s00410-011-0606-7.
Peng, G., Luhr, J.F., McGee, J.J., 1997. Factors controlling sulfur concentrations in volcanic apatite. Am. Mineral. 82 (11-12), 1210–1224. https://doi.org/10.2138/am-1997-11-1217.
Proffett, J.M., 2009. High Cu grades in porphyry Cu deposits and their relationship to emplacement depth of magmatic sources. Geology 37 (8), 675–678. https://doi.org/10.1130/G30072A.110.1130/2009163.
Prowatke, S., Klemme, S., 2006. Trace element partitioning between apatite and silicate melts. Geochim. Cosmochim. Acta 70 (17), 4513–4527. https://doi.org/10.1016/j.gca.2006.06.162.
Qin, Z.W., Lu, F.Q., Anderson, A.T., 1992. Diffusive reequilibration of melt and fluid inclusions. Am. Mineral. 77, 565–576.
Reid, A., Wilson, C.J.L., Shun, L., Pearson, N., Belousova, E., 2007. Mesozoic plutons of the Yidun Arc, SW China: U/Pb geochronology and Hf isotopic signature. Ore Geol. Rev., Special Issue on Mineral Deposits of South China 31, 88–106. https://doi.org/10.1016/j.oregeorev.2004.11.003.
Ridolfi, F., Renzulli, A., Puerini, M., 2010. Stability and chemical equilibrium of amphibole in calc-alkaline magmas: an overview, new thermobarometric formulations and application to subduction-related volcanoes. Contrib. Mineral. Petrol. 160 (1), 45–66. https://doi.org/10.1007/s00410-009-0465-7.
Riker, J., Humphreys, M.C., Brooker, R.A., De Hoog, J.C., EIMF, 2018. First measurements of OH-C exchange and temperature-dependent partitioning of OH and halogens in the system apatite–silicate melt. Am. Mineral. J. Earth Planet. Mater. 103, 260–270. https://doi.org/10.2138/am-2018-6187CCBY.
Sato, H., Holtz, F., Botcharnikov, R.E., Nakada, S., 2017. Intermittent generation of mafic enclaves in the 1991–1995 dacite of Unzen Volcano recorded in mineral chemistry. Contrib. Mineral. Petrol. 172, 22. https://doi.org/10.1007/s00410-017-1335-3.
Schmidt, M.W., 1992. Amphibole composition in tonalite as a function of pressure: an experimental calibration of the Al-in-hornblende barometer. Contrib. Mineral. Petrol. 110 (2-3), 304–310. https://doi.org/10.1007/BF00310745.
Scott, S., Driesner, T., Weis, P., 2015. Geologic controls on supercritical geothermal resources above magmatic intrusions. Nat. Commun. 6, 7837. https://doi.org/10.1038/ncomms8837.
Sha, L.K., Chappell, B.W., 1999. Apatite chemical composition, determined by electron microprobe and laser-ablation inductively coupled plasma mass spectrometry, as a probe into granite petrogenesis. Geochim. Cosmochim. Acta 63 (22), 3861–3881. https://doi.org/10.1016/S0016-7037(99)00210-0.
Sillitoe, R.H., 2010. Porphyry copper systems. Econ. Geol. 105 (1), 3–41. https://doi.org/10.2113/gsecongeo.105.1.3.
Stock, M.J., Humphreys, M.C., Smith, V.C., Isaia, R., Brooker, R.A., Pyle, D.M., 2018. Tracking volatile behaviour in sub-volcanic plumbing systems using apatite and glass: insights into pre-eruptive processes at Campi Flegrei. Italy. J. Petrol. 59, 2463–2492. https://doi.org/10.1093/petrology/egy020.
Streck, M.J., Dilles, J.H., 1998. Sulfur evolution of oxidized arc magmas as recorded in apatite from a porphyry copper batholith. Geology 26, 523–526. https://doi.org/10.1130/0091-7613(1998)026<0523:SEOOAM>2.3.CO;2.
Uchida, E., Endo, S., Makino, M., 2007. Relationship between solidification depth of granitic rocks and formation of hydrothermal ore deposits. Resour. Geol. 57 (1), 47–56. https://doi.org/10.1111/j.1751-3928.2006.00004.x.
Van Hoose, A.E., Streck, M.J., Pallister, J.S., Wälle, M., 2013. Sulfur evolution of the 1991 Pinatubo magmas based on apatite. J. Volcanol. Geotherm. Res. 257, 72–89. https://doi.org/10.1016/j.jvolgeores.2013.03.007.
Wang, B.Q., Zhou, M.F., Li, J.W., Yan, D.P., 2011. Late Triassic porphyritic intrusions and associated volcanic rocks from the Shangri-La region, Yidun terrane, Eastern Tibetan Plateau: adakitic magmatism and porphyry copper mineralization. Lithos 127 (1–2), 24–38. https://doi.org/10.1016/j.lithos.2011.07.028.
Wang, D.Z., Hu, R.Z., Hollings, P., Bi, X.W., Zhong, H., Pan, L.C., Leng, C.B., Huang, M.L., Zhu, J.J., 2021. Remelting of a Neoproterozoic arc root: origin of the Pulang and Songnuo porphyry Cu deposits, Southwest China. Miner. Deposita. https://doi.org/10.1007/s00126-021-01049-0.
Wang, P., Dong, G.C., Zhao, G.C., Han, Y.G., Li, Y.P., 2018. Petrogenesis of the Pulang porphyry complex, southwestern China: Implications for porphyry copper metallogenesis and subduction of the Paleo-Tethys Oceanic lithosphere. Lithos 304-307, 280–297.
Webster, J.D., Tappen, C.M., Mandeville, C.W., 2009. Partitioning behavior of chlorine and fluorine in the system apatite–melt–fluid. II: Felsic silicate systems at 200 MPa. Geochim. Cosmochim. Acta 73 (3), 559–581. https://doi.org/10.1016/j.gca.2008.10.034.
Webster, J.D., Piccoli, P.M., 2015. Magmatic apatite: A powerful, yet deceptive, mineral. Elements 11 (3), 177–182. https://doi.org/10.2113/gselements.11.3.177.
Wones, D., Eugster, H., 1965. Stability of biotite: experiment, theory, and application. Am. Mineral. J. Earth Planet. Mater. 50, 1228–1272.
Woodland, A.B., Wood, B.J., 1994. Fe3O4 activities in Fe-Ti spinel solid solutions. Eur. J. Mineral. 6 (1), 23–38. https://doi.org/10.1127/ejm/6/1/0023.
Xing, K., Shu, Q.H., Zhao, H.S., Xu, H.N., 2018. Geochemical characteristics and geological significance of apatites in the Pulang porphyry copper deposit, NW Yunnan Province. Acta Petrol. Sin. 34, 1427–1440 (in Chinese with English abstract).
Xing, K., Shu, Q., Lentz, D.R., 2021. Constraints on the Formation of the Giant Daheishan Porphyry Mo Deposit (NE China) from Whole-Rock and Accessory Mineral Geochemistry. J. Petrol. 62 https://doi.org/10.1093/petrology/egab018.
Xing, K., Shu, Q., Lentz, D.R., Wang, F., 2020. Zircon and apatite geochemical constraints on the formation of the Huojihe porphyry Mo deposit in the Lesser Xing'an Range, NE China. Am. Mineral. 105, 382–396. https://doi.org/10.2138/am-2020-7226.

Xu, B., Hou, Z.Q., Griffin, W.L., Lu, Y., Belousova, E., Xu, J.F., O'Reilly, S.Y., 2021. Recycled volatiles determine fertility of porphyry deposits in collisional settings. Am. Mineral. J. Earth Planet. Mater. 106, 656–661. https://doi.org/10.2138/am-2021-7714.

Yang, L.Q., Deng, J., Dilek, Y., Meng, J.Y., Gao, X., Santosh, M., Wang, D., Yan, H., 2016. Melt source and evolution of I-type granitoids in the SE Tibetan Plateau: Late Cretaceous magmatism and mineralization driven by collision-induced transtensional tectonics. Lithos 245, 258–273. https://doi.org/10.1016/j.lithos.2015.10.005.

Yang, L.Q., Gao, X., Shu, Q.H., 2017. Multiple Mesozoic porphyry-skarn Cu (Mo–W) systems in Yidun Terrane, east Tethys: constraints from zircon U-Pb and molybdenite Re–Os geochronology. Ore Geol. Rev. 90, 813–826. https://doi.org/10.1016/j.oregeorev.2017.01.030.

Yang, L.Q., He, W.Y., Gao, X., Xie, S.X., Yang, Z., 2018. Mesozoic multiple magmatism and porphyry–skarn Cu–polymetallic systems of the Yidun Terrane, Eastern Tethys: implications for subduction-and transtension-related metallogeny. Gondwana Res. 62, 144–162. https://doi.org/10.1016/j.gr.2018.02.009.

Yang, Z.M., Cooke, D.R., 2019. Porphyry Cu Deposits in China. Soc. Econ. Geol. Spec. Publ. 22, 133–187. https://doi.org/10.5382/SP.22.05.

Zajacz, Z., Candela, P.A., Piccoli, P.M., Sanchez-Valle, C., 2012. The partitioning of sulfur and chlorine between andesite melts and magmatic volatiles and the exchange coefficients of major cations. Geochim. Cosmochim. Acta 89, 81–101. https://doi.org/10.1016/j.gca.2012.04.039.